ORIGINAL ARTICLE

Rupert Klein

Asymptotics, structure, and integration of sound-proof atmospheric flow equations

Abstract Relative to the full compressible flow equations, sound-proof models filter acoustic waves while maintaining advection and internal waves. Two well-known sound-proof models, an anelastic model by Bannon and Durran's pseudo-incompressible model, are shown here to be structurally very close to the full compressible flow equations. Essentially, the anelastic model is obtained by suppressing $\partial_t \rho$ in the mass continuity equation and slightly modifying the gravity term, whereas the pseudo-incompressible model results from dropping $\partial_t p$ from the pressure equation. For length scales small compared to the density and pressure scale heights, the anelastic model reduces to the Boussinesq approximation, while the pseudo-incompressible model approaches the zero Mach number, variable density flow equations. Thus, for small scales, both models are asymptotically consistent with the full compressible flow equations, yet the pseudo-incompressible model is more general in that it remains valid in the presence of large density variations. For the relatively small density variations found in typical atmosphere–ocean flows, both models are found to yield very similar results, with deviations between models much smaller than deviations obtained when using different numerical schemes for the same model. This in agreement with Smolarkiewicz and Dörnbrack (Int J Numer Meth Fluids 56:1513–1519, 2007). Despite these useful properties, neither model can be derived by a low-Mach number asymptotic expansion for length scales comparable to the pressure scale height, i.e., for the regime they were originally designed for. Derivations of these models via scale analysis ignore an asymptotic time scale separation between advection and internal waves. In fact, only the classical Ogura and Phillips model, which assumes weak stratification of the order of the Mach number squared, can be obtained as a leading-order model from systematic low Mach number asymptotic analysis. Issues of formal asymptotics notwithstanding, the close structural similarity of the anelastic and pseudo-incompressible models to the full compressible flow equations makes them useful limit systems in building computational models for atmospheric flows. In the second part of the paper, we propose a second-order finite-volume projection method for the anelastic and pseudo-incompressible models that observes these structural similarities. The method is applied to test problems involving free convection in a neutral atmosphere, the breaking of orographic waves at high altitudes, and the descent of a cold air bubble in the small-scale limit. The scheme is meant to serve as a starting point for the development of a robust compressible atmospheric flow solver in future work.

Keywords Meteorology · Anelastic models · Low Mach number asymptotics · Finite volume projection method

PACS 92.60.Aa

R. Klein
FB Mathematik and Informatik, Freie Universität Berlin, Berlin, Germany
E-mail: rupert.klein@zib.de

1 Introduction

Sound waves are considered unimportant for most atmospheric flow applications, yet they provide for technical difficulties in numerical solutions of the compressible flow equations in atmospherically relevant flow regimes due to their fast characteristic time scale. The quest for efficient ways of handling these difficulties is ongoing (see, e.g., [7,19–23,29,39,49] and references therein). An alternative to solving the full compressible flow equations is to adopt approximate sound-proof model equations. These anelastic, [4,18,32,37] or pseudo-incompressible [16,17] models involve a velocity divergence constraint which eliminates the undesired sound modes while maintaining the meteorologically important advection and internal gravity wave modes. The numerical methods used to integrate these sound-proof models are relatives of incompressible Euler and high-Reynolds number Navier–Stokes flow solvers as exemplified, e.g., in [2,20,43,47,49]. The scheme in [20] is an example of an all-speed solver designed to smoothly cover the transition from weakly compressible to sound-proof flow regimes. In a similar fashion, the method by Janjic et al. [23], solves the compressible and the hydrostatic primitive equations within a unified numerical framework.

For flows on length scales that are small compared to the atmospheric pressure scale height, the two most frequently used sound-proof models are the Boussinesq approximation and the equations for incompressible variable density flows. Formal asymptotic and rigorous analyses demonstrate how these reduced models can be derived from the full compressible flow equations in the limit of vanishing Mach number (see, e.g., [42,53,57], and references therein). One representative of the family of anelastic models by Bannon, [4], is shown here to reduce to the Boussinesq model for sufficiently small scales. In contrast, Durran's pseudo-incompressible model [16], approaches the more general equations for incompressible variable density flows in this limit. Thus, for small scales, both Bannon's anelastic and Durran's pseudo-incompressible models are asymptotically consistent with the compressible Euler equations in the limit of vanishing Mach number, M, albeit in different regimes for variations of density or, equivalently in this case, potential temperature.

In contrast, for meteorologically relevant length and time scales comparable to 10 km and 20 min or larger, the relation between the full compressible flow equations and the anelastic or pseudo-incompressible models is less clear. By reconsidering the low Mach number analysis in [26], we demonstrate here that only the classical anelastic model by Ogura and Phillips [37], which assumes weak potential temperature stratification of order $O(\mathrm{M}^2)$, can be derived from the compressible flow equations through systematic scale analysis or asymptotics. In contrast, the generalizations in [4,16,18,32] which allow for more realistic stronger stratification cannot be justified in this way. Because of an asymptotic time scale separation between advection and internal wave motions that arises for such stronger stratifications, derivations that would simultaneously incorporate both these processes would have to explicitly adopt multiple time and/or multiple spacial scales. Models that do not address this scale separation represent compositions of lower- and higher-order terms, whose (temporal) range of validity remains unclear.

Nevertheless, consider the full compressible flow equations as obtained for $\alpha = 1$ from

$$\rho_t + \nabla \cdot (\rho \boldsymbol{v}) = 0$$
$$(\rho \boldsymbol{v})_t + \nabla \cdot (\rho \boldsymbol{v} \circ \boldsymbol{v}) + P \nabla \pi = -\rho g \boldsymbol{k} \tag{1}$$
$$\alpha P_t + \nabla \cdot (P \boldsymbol{v}) = 0.$$

These are the Euler equations in non-dimensional form for an ideal gas with constant specific heat capacities with $\rho, \boldsymbol{v}, P, \pi$ denoting density, velocity, and the pressure-related variables,

$$P = p^{\frac{1}{\gamma}} = \rho \theta, \quad \pi = \Gamma^{-1} p^{\Gamma}, \quad \Gamma = \frac{\gamma - 1}{\gamma}, \tag{2}$$

with p, θ the pressure and potential temperature, and γ the isentropic exponent. The anelastic and pseudo-incompressible models not only share the two principal meteorologically relevant fluid dynamical processes of advection and internal waves with (1), but they are also structurally very similar. In fact, as we will demonstrate here, one obtains, e.g., Durran's pseudo-incompressible flow equations by simply setting $\alpha = 0$ in $(1)_3$ and assigning $P \equiv \overline{P}(z)$ to its hydrostatic background distribution. Of course, the definitions in (2) cease to be valid in that case, and π assumes its usual role as a Lagrange multiplier that guarantees compliance with the divergence constraint $\nabla \cdot (\overline{P} \boldsymbol{v}) = 0$. Analogous explanations are given in Sect. 2.4.1 for the relation of Bannon's anelastic model to (1).

We intend to exploit this structural similarity in designing a family of atmospheric flow solvers which address anelastic, pseudo-incompressible, and fully compressible flows within a single numerical framework and with minimal modifications needed to switch between these versions. In Sect. 3 below, we start the development with an anelastic/pseudo-incompressible solver based on Godunov-type finite volume techniques.

The scheme provides the following features:

1. Mass conservation,
2. Stability for advection Courant number close to unity,
3. Accuracy of advection independent of the velocity divergence,
4. Conceptually straight-forward extension to the full compressible flow equations,
5. Accuracy independent of whether or not a background mean state is subtracted.

To achieve these, we devise a second-order projection method following ideas from [24,27,36,41]. The scheme combines a conservative Godunov-type predictor step for mass, momentum, potential temperature, and other advected scalars with two projections controlling compliance with the anelastic/pseudo-incompressible divergence constraints from [55,56]. This provides for mass conservation and allows advection Courant numbers close to unity. The predictor step solves an auxiliary hyperbolic equation system that does not involve a velocity divergence constraint. As in a compressible flow solver, advection is thus represented equally well for divergent and non-divergent flows (see also [6]). Also, (1) this provides robustness of the results with respect to the level of divergence-control in anelastic/pseudo-incompressible computations, (2) it reduces a subsequent extension of the scheme to the full compressible flow equations to the task of "merely" incorporating the $\partial_t P$ term in $(1)_3$, and (3) it prepares the ground for extensions to higher than second order through the spectral deferred correction time integration technique from [24].

The predictor step can be implemented using a range of conservative advective transport schemes and different time integrators. Here we opt for simplicity and combine second-order Godunov-type MUSCL (Monotone Upstream Scheme for Conservation Laws) techniques (see, e.g., [31,35,54]) with Strang splitting [50], to account for multiple dimensions. Standard TVD slope limiters as used in the MUSCL-scheme are known to clip extrema of advected quantities. This turns out to be detrimental, e.g., in the "rising-bubble" test discussed in Sect. 4.2 below. Improved results are obtained using (unlimited) upwind-biased piecewise parabolic reconstruction [14], combined with a simple plateau-detection scheme. We describe a preliminary implementation of the scheme in the Appendix and use it to demonstrate the effects of clipping of extrema. A detailed discussion of the advection scheme is deferred to a separate publication. The reader may also want to consult [6] for a detailed discussion of a very similar approach to advection.

Implementing the gravity source term, we adopt the well-balanced discretization based on local hydrostatic reconstruction which was first described by Botta et al. [10] in the context of an explicit compressible Euler solver. As in that paper, we achieve here a discretization that does not require subtraction of a hydrostatic background state to achieve full accuracy. Without penalty, the scheme may, but does not have to, be run advecting the full potential temperature and using the full pressure field.

We should mention that Gatti-Bono and Colella, [20], substantially extending and then implementing ideas from [26], propose a strategy for constructing all-speed atmospheric flow solvers that separately handle sound waves, internal gravity waves, and advection in the discretization. This approach is thus designed in principle to account for the time scale separation between advection and internal waves mentioned above, although that was not yet achieved in [20].

In Sect. 2, we summarize the various flow models discussed in this paper as well as their asymptotics and structure. In Sect. 3, we propose the numerical flow solver. Section 4, we demonstrate properties of the models and of the numerical scheme using three test cases: the breaking of lee waves at high altitudes, the rising of a hot air bubble in a neutrally stratified deep atmosphere, and the descent of cold air patches of various temperatures in a small box of neutrally stratified gas.

2 Compressible, anelastic, and pseudo-incompressible flow models

2.1 Compressible Euler equations

The dimensionless mass, momentum, and energy balances for an ideal gas with constant heat capacities under the influence of gravity read

Compressible Euler equations

$$\rho_t + \nabla \cdot (\rho \boldsymbol{v}) = 0$$
$$(\rho \boldsymbol{v})_t + \nabla \cdot (\rho \boldsymbol{v} \circ \boldsymbol{v}) + \nabla p = -\rho g \boldsymbol{k} \quad (3)$$
$$(\rho E)_t + \nabla \cdot (\boldsymbol{v}[\rho E + p]) = 0,$$

where

$$\rho E = \frac{p}{\gamma - 1} + \frac{\rho \boldsymbol{v}^2}{2} + \rho g z. \quad (4)$$

Here $\rho, p, \boldsymbol{v}$ are density, pressure, and the flow velocity vector, respectively, g is the gravitational acceleration, γ the isentropic exponent, z the vertical space coordinate, and "$\circ$" denotes the tensorial product. We think of $[p, \rho, \boldsymbol{v}, g]$, and the independent variables $[t, (x, y, z)]$ in (3) as nondimensionalized by $[p_{\mathrm{ref}}, \rho_{\mathrm{ref}}, c_{\mathrm{ref}}, c_{\mathrm{ref}}^2/\ell_{\mathrm{ref}}]$, and $[\ell_{\mathrm{ref}}/c_{\mathrm{ref}}, \ell_{\mathrm{ref}}]$, respectively, where $c_{\mathrm{ref}} = \sqrt{p_{\mathrm{ref}}/\rho_{\mathrm{ref}}}$ is of the order of the speed of sound, and

$$\ell_{\mathrm{ref}} = \frac{p_{\mathrm{ref}}}{\rho_{\mathrm{ref}} \, g_{\mathrm{ref}}} = h_{\mathrm{sc}} \quad (5)$$

is the pressure scale height.

For flows without shocks, two equivalent equations can be derived that we will use below to replace the energy conservation law (3)$_3$,

$$(\rho\theta)_t + \nabla \cdot (\rho\theta \boldsymbol{v}) = 0, \quad \left(\theta = p^{\frac{1}{\gamma}}/\rho\right)$$
$$P_t + \nabla \cdot (P\boldsymbol{v}) = 0, \quad \left(P \equiv p^{\frac{1}{\gamma}}\right). \quad (6)$$

Equation (6)$_1$ may be interpreted as expressing the first law of thermodynamics for an adiabatic fluid. It may also be interpreted as a transport equation in conservation form for the potential temperature, θ, and this will be important in the sequel. Equation (6)$_2$ is a somewhat unusual way of writing the more familiar non-conservative pressure equation for an adiabatic fluid

$$p_t + \boldsymbol{v} \cdot \nabla p + \gamma p \nabla \cdot \boldsymbol{v} = 0. \quad (7)$$

Also, for flows without shocks, the momentum equation, (3)$_2$, may be rewritten as

$$(\rho \boldsymbol{v})_t + \nabla \cdot (\rho \boldsymbol{v} \circ \boldsymbol{v}) + \rho\theta\nabla\pi = -g\boldsymbol{k}, \quad (8)$$

where

$$\pi = \Gamma^{-1} p^{\Gamma}, \quad \text{with} \quad \Gamma = \frac{\gamma - 1}{\gamma}, \quad (9)$$

is proportional to the Exner pressure variable, p^{Γ}.

While it is clear that shock waves must be excluded when adopting (6) and (8) instead of the mass, momentum, and energy conservation laws, it seems likely that contact discontinuities, i.e., discontinuities of θ, would still be allowed. Addressing this question is beyond the scope of the present paper.

2.2 Ogura and Phillips' (1962) anelastic model

2.2.1 Asymptotic derivation

In their seminal paper [37], Ogura and Phillips derive a reduced system of equations from (3) through scale analysis based on the limit of vanishing Mach number. To summarize their analysis, we consider flow velocities much smaller than the speed of sound, and nondimensionalize velocity and time by

$$u_{\mathrm{ref}} = \mathrm{M}c_{\mathrm{ref}}, \quad t_{\mathrm{ref}} = \frac{h_{\mathrm{sc}}}{u_{\mathrm{ref}}}, \quad \text{with} \quad (\mathrm{M} \ll 1). \quad (10)$$

With this rescaling and using $(6)_1$ instead of energy conservation, the governing equations from (3) become

$$\rho_t + \nabla \cdot (\rho \boldsymbol{v}) = 0$$

$$(\rho \boldsymbol{v})_t + \nabla \cdot (\rho \boldsymbol{v} \circ \boldsymbol{v}) + \frac{1}{\mathrm{M}^2} \nabla p = -\frac{g}{\mathrm{M}^2} \rho \boldsymbol{k} \qquad (11)$$

$$(\rho \theta)_t + \nabla \cdot (\rho \theta \boldsymbol{v}) = 0.$$

If we do not allow for a further rescaling of the space or time coordinates with M, i.e., if we restrict ourselves to the Lagrangian time scale for flows over distances of $O(h_{\mathrm{sc}})$ as $\mathrm{M} \to 0$, then the momentum equation and the thermodynamic relationship, $\rho \theta = p^{1/\gamma}$, require

$$\rho(\boldsymbol{x}, t; \mathrm{M}) = \overline{\rho}(z) + \mathrm{M}^2 \rho'(\boldsymbol{x}, t) + o(\mathrm{M}^2)$$

$$p(\boldsymbol{x}, t; \mathrm{M}) = \overline{p}(z) + \mathrm{M}^2 p'(\boldsymbol{x}, t) + o(\mathrm{M}^2) \quad \text{as} \quad (\mathrm{M} \to 0) \qquad (12)$$

$$\theta(\boldsymbol{x}, t; \mathrm{M}) = \overline{\theta}(z) + \mathrm{M}^2 \theta'(\boldsymbol{x}, t) + o(\mathrm{M}^2).$$

and

$$\boldsymbol{v}(\boldsymbol{x}, t; \mathrm{M}) = \boldsymbol{v}_0(\boldsymbol{x}, t) + o(1), \quad \text{as} \quad (\mathrm{M} \to 0). \qquad (13)$$

Subtracting the leading-order hydrostatic balance

$$\frac{\mathrm{d}\overline{p}}{\mathrm{d}z} = -\overline{\rho} g, \quad \overline{\rho}\overline{\theta} = \overline{p}^{\frac{1}{\gamma}} \qquad (14)$$

from $(11)_2$ and dropping higher-order terms, we find the rescaled leading-order evolution equations

$$\nabla \cdot (\overline{\rho} \boldsymbol{v}_0) = 0$$

$$(\rho \boldsymbol{v}_0)_t + \nabla \cdot (\rho \boldsymbol{v}_0 \circ \boldsymbol{v}_0) + \nabla p' = \overline{\rho} \left(\frac{\theta'}{\overline{\theta}} - \frac{p'}{\gamma \overline{p}} \right) g \boldsymbol{k} \qquad (15)$$

$$\theta'_t + \boldsymbol{v}_0 \cdot \nabla \theta' + \frac{S}{\mathrm{M}^2} \overline{\theta} \, w_0 = 0$$

with the local stability

$$S = \frac{1}{\overline{\theta}} \frac{\mathrm{d}\overline{\theta}}{\mathrm{d}z}. \qquad (16)$$

Equation $(15)_3$ forces us to either accept $w_0 \equiv 0$, which would suppress internal waves, or to restrict ourselves to weak stratification with $S = O(\mathrm{M}^2)$ as $\mathrm{M} \to 0$. For a discussion of the former regime see, e.g., [26,33,57]. The latter regime was considered by Ogura and Phillips [37], and leads to the classical anelastic model with a homentropic background stratification,

$$\overline{\rho}(z) = \overline{p}(z)^{\frac{1}{\gamma}} = (1 - \Gamma g z)^{\frac{1}{\gamma \Gamma}}. \qquad (17)$$

More specifically, dropping the $_0$-subscript, we have the
Ogura and Phillips' model

$$\nabla \cdot (\overline{\rho} \boldsymbol{v}) = 0$$

$$(\overline{\rho} \boldsymbol{v})_t + \nabla \cdot (\overline{\rho} \boldsymbol{v} \circ \boldsymbol{v}) + \overline{\rho} \nabla \pi' = g \overline{\rho} \theta' \boldsymbol{k} \qquad (18)$$

$$(\overline{\rho} \theta')_t + \nabla \cdot (\overline{\rho} \theta' \boldsymbol{v}) = 0.$$

Without (further) loss of generality we have assumed

$$\theta = 1 + \mathrm{M}^2 \theta' + o(\mathrm{M}^2), \qquad (19)$$

thereby absorbing the weak background stratification in θ', and introduced the scaled pressure perturbation

$$\pi' = \frac{p'}{\overline{\rho}}, \qquad (20)$$

Table 1 Characteristic inverse time scales

	Dimensional	Dimensionless
Advection	$\frac{u_{\text{ref}}}{h_{\text{sc}}}$	1
Internal waves	$N = \sqrt{\frac{g}{\theta}\frac{\mathrm{d}\overline{\theta}}{\mathrm{d}z}}$	$\frac{\sqrt{gh_{\text{sc}}}}{u_{\text{ref}}}\sqrt{\frac{h_{\text{sc}}}{\overline{\theta}}\frac{\mathrm{d}\overline{\theta}}{\mathrm{d}z}} = \frac{1}{\text{M}}\sqrt{\frac{h_{\text{sc}}}{\overline{\theta}}\frac{\mathrm{d}\overline{\theta}}{\mathrm{d}z}}$
Sound	$\frac{\sqrt{gh_{\text{sc}}}}{h_{\text{sc}}}$	$\frac{\sqrt{gh_{\text{sc}}}}{u_{\text{ref}}} = \frac{1}{\text{M}}$

so that

$$\overline{\rho}(\nabla\pi' - g\theta'\boldsymbol{k}) = \nabla p' + g\overline{\rho}\left(\frac{p'}{\gamma\overline{p}} - \frac{\theta'}{\overline{\theta}}\right)\boldsymbol{k} \tag{21}$$

as required by (15)$_2$. In deriving (21) we have used

$$\overline{\rho}\frac{\mathrm{d}}{\mathrm{d}z}\frac{1}{\overline{\rho}} = -\frac{1}{\overline{\rho}}\left(\frac{\partial\rho}{\partial p}\right)_\theta\frac{\mathrm{d}\overline{p}}{\mathrm{d}z} = \frac{g}{\gamma\overline{p}}, \quad \text{where} \quad \left(\frac{\partial\rho}{\partial p}\right)_\theta = \frac{\overline{\rho}}{\gamma\overline{p}}, \quad \frac{\mathrm{d}\overline{p}}{\mathrm{d}z} = -g\overline{\rho}. \tag{22}$$

For later reference, note that due to (17) the anelastic divergence constraint in (18)$_1$ is equivalent to the pseudo-incompressible one in the weak stratification regime, i.e.,

$$\nabla\cdot\left(\overline{p}^{\frac{1}{\gamma}}\boldsymbol{v}\right) = \nabla\cdot(\overline{\rho}\overline{\theta}\boldsymbol{v}) = \nabla\cdot(\overline{P}\boldsymbol{v}) = 0. \tag{23}$$

2.2.2 Remarks on asymptotic models for stronger stratification

In deriving a model that is sound-proof but does incorporate advection and internal waves on the same length and time scales, we were forced to adopt asymptotically weak stratification. To corroborate this from a physical point of view, Table 1 compares the characteristic time scales of these three processes, both in dimensional and non-dimensional terms (notice that $gh_{\text{sc}} = p_{\text{ref}}/\rho_{\text{ref}} \sim c_{\text{ref}}$).

As $\text{M} \to 0$, the characteristic frequency of internal waves is of the same order as the inverse of the characteristic time of sound wave propagation unless we assume weak stratification $\mathrm{d}\overline{\theta}/\mathrm{d}z = O(\text{M}^2)$. For stronger stratification and on the Lagrangian advection time scale, both sound waves and internal waves get eliminated in the low Mach number limit, and one obtains model equations for buoyancy-controlled flow, [8,26,28,33,57], also known as the Weak Temperature Gradient approximation (WTG), [48]. The leading-order model, in the presence of diabatic heating S_θ, in this case reads,

$$\boldsymbol{u}_t + \boldsymbol{u}\cdot\nabla_\parallel\boldsymbol{u} + \overline{\theta}\nabla_\parallel\pi = 0$$
$$\rho_0\nabla_\parallel\cdot\boldsymbol{u} + (\rho_0 w)_z = 0$$
$$w = \frac{S_\theta}{\mathrm{d}\overline{\theta}/\mathrm{d}z}.$$

Here $\boldsymbol{u}$, w denote the horizontal and vertical velocity components, respectively, $\overline{\theta}(z)$ is the background stratification of potential temperature, and $\nabla_\parallel$ is the gradient operator w.r.t. the horizontal coordinates only [26]. This set of equations excludes both sound and internal waves.

If, again for stronger stratification, we were to adopt the internal wave time scale, i.e., the inverse of the characteristic frequency mentioned above, in constructing a reduced low Mach number model, then advection would be asymptotically slow in the limit, and the leading-order model would describe linearized internal waves but would exclude advection. See [28] for a related derivation including moisture effects. The leading-order model in this case reads,

$$\boldsymbol{u}_t + \nabla_\parallel\pi = 0$$
$$w_t + \pi_z = \theta'$$
$$\theta'_t + w\frac{d\overline{\theta}}{dz} = S_\theta$$
$$\rho_0\nabla_\parallel\cdot\boldsymbol{u} + (\rho_0 w)_z = 0.$$

This model describes internal gravity waves, while it excludes the effects of sound propagation and advection.

Of course, one could develop an asymptotic model that includes both advection and internal waves in a regime with stratification stronger than $O(\text{M}^2)$ by using techniques of multiple scales asymptotics. While this would surely be a worthwhile endeavour, it would not provide a set of equations that is structurally similar to the anelastic or pseudo-incompressible models. Rather, one would obtain two sets of equations, one for the fast, one for the slow components of the flow, together with suitable prescriptions for their coupling derived via the standard secular (sublinear growth) conditions.

We conclude:

1. It is not possible to derive a sound-proof model incorporating advection and internal waves for dimensionless stabilities stronger than $O(\text{M}^2)$ through single-scale asymptotics (or classical scale analysis).
2. The leading-order model for $O(\text{M}^2)$ stratification is that of Ogura and Phillips [37].

Bannon observes in [4] that one can systematically derive anelastic models for the entire range of stratifications from homentropic to isothermal provided one is willing to asymptotically constrain the fluid's equations of state. Thus, e.g., for an isothermal background state we have

$$\overline{p}(z) = \overline{\rho}(z) = \exp(-z), \quad \text{and} \quad \overline{\theta}(z) = \exp(\Gamma z). \tag{24}$$

In this case, one obtains weak stratifciation with $\mathrm{d}\overline{\theta}/\mathrm{d}z = O(\text{M}^2)$, if

$$\Gamma = (\gamma - 1)/\gamma = O(\text{M}^2) \quad \text{as} \quad (\text{M} \to 0). \tag{25}$$

While this limit does enable a systematic derivation of an anelastic model for flows in the homentropic-to-isothermal range, and while it is particularly useful in asymptotic analyses of diabatic flows [28,38], it does not change the previous conclusion that the resulting leading-order flow model is that of Ogura and Phillips [37].

2.3 Anelastic and pseudo-incompressible models

2.3.1 Dutton and Fichtl (1969), Lipps and Hemler (1982), Bannon (1996)

The Ogura and Phillips model is attactive because it filters the fast sound waves while maintaining advection of momentum and entropy and supporting internal gravity waves. It is criticized by practitioners, however, on the basis of the expansion scheme for potential temperature in (19) which restricts variations of the (dimensional) background potential temperature to unrealistically small values of $\text{M}^2\theta' p_{\text{ref}}/R\rho_{\text{ref}} \lesssim 1$ K. Realistic variations of potential temperature across the troposphere are instead of the order of 30–50 K.

This drawback has motivated a number of researchers to suggest extensions of this classical model that would render it applicable to flows with stronger stratification. Bannon [4], combining developments by Dutton and Fichtl [18], and Lipps and Hemler [32], proposed

Bannon's anelastic model

$$\nabla \cdot (\overline{\rho}\boldsymbol{v}) = 0$$

$$(\overline{\rho}\boldsymbol{v})_t + \nabla \cdot (\overline{\rho}\boldsymbol{v} \circ \boldsymbol{v}) + \overline{\rho}\nabla\pi' = g\overline{\rho}\frac{\theta - \overline{\theta}}{\overline{\theta}}\boldsymbol{k} \tag{26}$$

$$(\overline{\rho}\theta)_t + \nabla \cdot (\overline{\rho}\theta\boldsymbol{v}) = 0.$$

Here $\pi' = p'/\overline{\rho}$ is a scaled perturbation pressure, and $\overline{\theta}(z)$ is the desired z-dependent background stratification of potential temperature. By assuming a time-independent hydrostatic background density distribution,

$$\overline{\rho}(z) = \frac{\overline{p}(z)^{\frac{1}{\gamma}}}{\overline{\theta}(z)} = \frac{1}{\overline{\theta}(z)}\left(1 - \frac{\gamma - 1}{\gamma}g\int\limits_0^z \frac{1}{\overline{\theta}(z')}\,\mathrm{d}z'\right)^{\frac{1}{\gamma\Gamma}}, \tag{27}$$

the full continuity equation from (3)$_1$ reduces to the divergence constraint in (26)$_1$, and sound waves are eliminated.

Bannon's model in (26) is structurally very similar to that of Ogura and Phillips from (18). The only obvious change concerns the buoyancy term: Ogura and Phillips linearize density perturbations relative to a constant background potential temperature, whereas Bannon linearizes w.r.t. a height-dependent background. For a given background distribution of the density, $\overline{\rho}(z)$, this would be the only difference between these models, however, the background density distributions in (17) and (27) also differ in general as they are based on constant and stratified background potential temperature distributions, respectively.

Pressure gradient and gravity terms. The combination of the pressure gradient and buoyancy terms in $(26)_2$ can be expanded to give

$$\overline{\rho}\left(\nabla\pi' - g\frac{\theta - \overline{\theta}}{\overline{\theta}}\boldsymbol{k}\right) = \nabla p' + g\overline{\rho}\left(\frac{p'}{\gamma\overline{p}} - \frac{\theta'}{\overline{\theta}}\right)\boldsymbol{k} + \frac{p'}{\overline{\theta}}\frac{\mathrm{d}\overline{\theta}}{\mathrm{d}z}\boldsymbol{k}. \tag{28}$$

The first two terms on the right hand side match those in (21) providing the linearized influences of pressure and potential temperature perturbations on the buoyancy. Yet, there is now the additional term, $\frac{p'}{\overline{\theta}}\frac{\mathrm{d}\overline{\theta}}{\mathrm{d}z}\boldsymbol{k}$, which is not consistent with a perturbation analysis of the pressure gradient and gravity terms. Bannon argues in [4] that his model is explicitly restricted to relatively weak stratifications with $\frac{h_{\mathrm{sc}}}{\overline{\theta}}\frac{\mathrm{d}\overline{\theta}}{\mathrm{d}z} \ll 1$, so that this erroneous term is small. In addition, he suggests a possible further improvement through a re-definition of the potential temperature perturbation variable

$$\frac{\theta'}{\overline{\theta}} = -\frac{p'}{\overline{\rho}g}\frac{1}{\overline{\rho}}\frac{\mathrm{d}\overline{\rho}}{\mathrm{d}z} - \frac{\rho'}{\overline{\rho}} \tag{29}$$

which turns the entire right hand side of (28) into $\nabla p' + g\rho'$. This modification amounts to a change of the thermodynamic equation of state.

In deriving (28) and in discussing (29) we have used

$$\overline{\rho}\frac{\mathrm{d}}{\mathrm{d}z}\frac{1}{\overline{\rho}} = -\frac{1}{\overline{\rho}}\left(\left(\frac{\partial\rho}{\partial p}\right)_\theta(\overline{p},\overline{\theta})\frac{\mathrm{d}\overline{p}}{\mathrm{d}z} + \left(\frac{\partial\rho}{\partial\theta}\right)_p(\overline{p},\overline{\theta})\frac{\mathrm{d}\overline{\theta}}{\mathrm{d}z}\right) = \frac{\overline{\rho}g}{\gamma\overline{p}} + \frac{1}{\overline{\theta}}\frac{\mathrm{d}\overline{\theta}}{\mathrm{d}z}. \tag{30}$$

2.3.2 Durran (1989)

Durran's model [16], is obtained from the compressible flow equations in (1) by assuming a time independent leading-order pressure instead of a time independent leading-order density. The pressure equation $(1)_3 (or (6)_2)$, then yields the pseudo-incompressible divergence constraint [8,9,26],

$$\nabla \cdot (\overline{P}\boldsymbol{v}) = \nabla \cdot (\overline{\rho\theta}\boldsymbol{v}) = 0. \tag{31}$$

Durran actually suggests a slightly different version of the divergence constraint, $\nabla \cdot (\overline{\rho}\overline{\theta}\boldsymbol{v}) = 0$, which is equivalent to the above at leading order only if the deviations of both density and potential temperature from their background values are small. See Sect. 2.4.3 on the small-scale limit for further discussion.

The pseudo-incompressible model is now obtained from the full compressible flow equations by replacing the energy conservation law with (31) and modifying the pressure gradient term as described shortly. Specifically, we have

Durran's pseudo-incompressible model

$$\rho_t + \nabla \cdot (\rho\boldsymbol{v}) = 0$$
$$(\rho\boldsymbol{v})_t + \nabla \cdot (\rho\boldsymbol{v} \circ \boldsymbol{v}) + \overline{P}\nabla\pi' = g\rho\frac{\theta - \overline{\theta}}{\overline{\theta}}\boldsymbol{k} \tag{32}$$
$$\nabla \cdot (\overline{P}\boldsymbol{v}) = 0,$$

where

$$\overline{P} = \overline{p}^{\frac{1}{\gamma}}, \quad \theta = \frac{\overline{P}}{\rho}, \quad \pi' = \pi - \overline{\pi} = \frac{1}{\Gamma}(p^\Gamma - \overline{p}^\Gamma). \tag{33}$$

The background pressure distribution, $\overline{p}(z)$, is assumed to satisfy

$$\overline{P}\frac{\mathrm{d}\overline{\pi}}{\mathrm{d}z} = \frac{\overline{P}}{\Gamma}\frac{\mathrm{d}\overline{p}^\Gamma}{\mathrm{d}z} = \frac{\gamma}{\gamma-1}\overline{p}^{\frac{1}{\gamma}}\frac{\mathrm{d}\overline{p}^{\frac{\gamma-1}{\gamma}}}{\mathrm{d}z} = \frac{\mathrm{d}\overline{p}}{\mathrm{d}z} = -g\overline{\rho} = -g\overline{p}^{\frac{1}{\gamma}}\overline{\left(\frac{1}{\theta}\right)}, \tag{34}$$

which yields

$$\overline{P}(z) = \overline{p}(z)^{\frac{1}{\gamma}} = \left(1 - \Gamma g \int\limits_0^z \overline{\left(\frac{1}{\theta}\right)}(z')\,\mathrm{d}z'\right)^{\frac{1}{\gamma\Gamma}}. \tag{35}$$

This is analogous to the background distributions in Ogura and Phillips' and Bannon's models, provided $1/\overline{\theta}(z)$ in (27) is replaced with $\overline{(1/\theta)}(z)$.

Advection of potential temperature. In the pseudo-incompressible model, (32), the mass conservation law is responsible for the advection of potential temperature. In fact, under the pertinent assumption that pressure variations are very small, the leading-order approximation to the thermodynamic relation reads

$$\rho = \overline{p}^{\frac{1}{\gamma}}/\theta, = \overline{P}/\theta \tag{36}$$

and, using the divergence constraint from (32)$_3$ in the continuity (32)$_1$, we find

$$(1/\theta)_t + \boldsymbol{v} \cdot \nabla(1/\theta) = 0. \tag{37}$$

Pressure gradient and gravity terms. The sum of the pressure gradient and gravity terms in (32) is

$$\overline{P}\nabla\pi' - g\rho\frac{\theta - \overline{\theta}}{\overline{\theta}}\boldsymbol{k} \approx \nabla p' + \boldsymbol{k}g\overline{\rho}\left(\left(\frac{\rho}{\overline{\rho}} - 1\right) + \frac{p'}{\gamma\overline{p}}\right). \tag{38}$$

In deriving (38) we have assumed that $\overline{\rho} = \overline{P}/\overline{\theta} = \overline{\rho\theta}/\overline{\theta}$, which is justified as long as variations of density and potential temperature remain small (see, however, also our remarks on the small-scale limit below). Furthermore, we have assumed that $\pi'/\overline{\pi} \ll 1$, and linearized the relation $\pi = p^\Gamma/\Gamma$, so that

$$\pi' = \frac{1}{\Gamma}(p^\Gamma - \overline{p}^\Gamma) = \overline{p}^{\Gamma-1}p' + o(p') = \frac{p'}{\overline{P}} + o(p') \quad \text{where} \quad p' = p - \overline{p}. \tag{39}$$

Durran [16], points out that the momentum equation of the pseudo-incompressible model in (32)$_2$ carries the fully nonlinear dependence of density on the potential temperature. From (38), we conclude that the influence of pressure perturbations on the density is included through a Boussinesq-type approximation: a linearized version of that influence is retained in the combination of the gravity and pressure gradient terms through the last term in (38) while it is otherwise neglected in the momentum balance.

2.4 Structural comparison of the three flow models

2.4.1 Non-perturbative form of the equations

The compressible Euler equations may be written as
Compressible Euler equations

$$\rho_t + \nabla \cdot (\rho\boldsymbol{v}) = 0$$
$$(\rho\boldsymbol{v})_t + \nabla \cdot (\rho\boldsymbol{v} \circ \boldsymbol{v}) + P\nabla\pi = -g\rho\boldsymbol{k} \tag{40}$$
$$P_t + \nabla \cdot (P\boldsymbol{v}) = 0$$

with $P = p^{1/\gamma} = \rho\theta$ and $\pi = p^\Gamma/\Gamma$ where $\Gamma = (\gamma - 1)/\gamma$. Durran's model is obtained from this system by simply dropping the pressure time derivative and assuming that P matches the prescribed background distribution $P \equiv \overline{P}(z)$ from (35). In fact, if we add the background hydrostatic balance to the momentum equation in (32), the pseudo-incompressible model becomes
Pseudo-incompressible model

$$\rho_t + \nabla \cdot (\rho\boldsymbol{v}) = 0$$
$$(\rho\boldsymbol{v})_t + \nabla \cdot (\rho\boldsymbol{v} \circ \boldsymbol{v}) + \overline{P}\nabla\pi = -g\rho\boldsymbol{k} \tag{41}$$
$$\nabla \cdot (\overline{P}\boldsymbol{v}) = 0.$$

Bannon's model is obtained from (40) by dropping the density time derivative, assuming $\rho \equiv \overline{\rho}(z)$ from (27), and slightly modifying the pressure gradient and gravity terms, and thus we have the
Anelastic model

$$\nabla \cdot (\overline{\rho} \boldsymbol{v}) = 0$$

$$(\overline{\rho} \boldsymbol{v})_t + \nabla \cdot (\overline{\rho} \boldsymbol{v} \circ \boldsymbol{v}) + \overline{\rho} \nabla \pi = -g \overline{\rho} \left(1 - \frac{\theta - \overline{\theta}}{\overline{\theta}} \right) \boldsymbol{k} \tag{42}$$

$$(\overline{\rho} \theta)_t + \nabla \cdot (\overline{\rho} \theta \boldsymbol{v}) = 0.$$

Here, we have replaced the pressure variable π' in (26) with

$$\pi = \pi' + \Pi \quad \text{with } \Pi \text{ satisfying} \quad \frac{\mathrm{d}\Pi}{\mathrm{d}z} = -g. \tag{43}$$

In Sect. 3 below, we will exploit the close structural similarity of these models to construct a numerical scheme that solves either of the two sound-proof sets of model equations using the same basic numerical techniques. For a subsequent paper, we plan to extend this solver to the case of (weakly) compressible flow in such a way that the sound-proof limits remain accessible. For a more comprehensive comparison of atmospheric flow models and their linearizations see Davies et al. [15].

2.4.2 Energy and pseudo-energy conservation

An important requirement for reduced flow models is that they do not exhibit spurious instabilities incompatible with the full model. One criterion that is generally checked is the conservation of a nonlinear energy for the full nonlinear models or a quadratic pseudo-energy for their linearized counterparts. Both Bannon's anelastic hybrid model and Durran's pseudo-incompressible model observe such conservation laws. The reader is referred to the original references for corroboration [4, 16].

2.4.3 Small-scale limits

In Sect. 2.2.1, we point out that the sound-proof models of the present section cannot have a systematic asymptotic derivation for stratifications $\frac{h_{\mathrm{sc}}}{\overline{\theta}} \frac{\mathrm{d}\overline{\theta}}{\mathrm{d}z} > O(\mathrm{M}^2)$. We now show that, nevertheless, both Bannon's and Durran's model do agree asymptotically with particular asymptotic low Mach number limits of the compressible flow equations when $\ell_{\mathrm{ref}} \ll h_{\mathrm{sc}}$. To verify this, we introduce the rescaled variables $(\hat{\rho}, \hat{\theta}, \hat{\boldsymbol{v}}, \hat{\pi}; \hat{t}, \hat{\boldsymbol{x}})$ defined by

$$(\rho, \theta, \boldsymbol{v}, \pi'; t, \boldsymbol{x}') = \left(\hat{\rho}, \hat{\theta}, \delta^{\frac{1}{2}} \hat{\boldsymbol{v}}, \delta \hat{\pi}; \delta^{\frac{1}{2}} \hat{t}, \delta \hat{\boldsymbol{x}} \right), \quad \delta = \frac{\ell_{\mathrm{ref}}}{h_{\mathrm{sc}}} \ll 1, \quad \boldsymbol{x}' = \boldsymbol{x} - \boldsymbol{x}_0, \tag{44}$$

where $\boldsymbol{x}_0$ is the center of the considered (small) flow domain. These new variables are chosen such that

1. $\hat{\boldsymbol{x}}$ resolves the new characteristic length ℓ_{ref},
2. $\hat{t}$ resolves the advective time scale in the rescaled system, so that

$$\left(\frac{\partial}{\partial t} + \boldsymbol{v} \cdot \nabla \right) = \delta^{-\frac{1}{2}} \left(\frac{\partial}{\partial \hat{t}} + \hat{\boldsymbol{v}} \cdot \hat{\nabla} \right), \tag{45}$$

and
3. accelerations retain their order of magnitude, since

$$\frac{\partial \boldsymbol{v}}{\partial t} = \delta^{\frac{1}{2}} \frac{\partial \hat{\boldsymbol{v}}}{\partial \hat{t}} \frac{d\hat{t}}{dt} = \frac{\partial \hat{\boldsymbol{v}}}{\partial \hat{t}}. \tag{46}$$

The pseudo-incompressible and anelastic models from (41) and (42) are invariant under this transformation, except for a δ-dependent re-interpretation of the background distributions $\overline{\rho}(z)$, $\overline{P}(z)$, and $\overline{\theta}(z)$, respectively. With the transformation $z = z_0 + \delta\hat{z}$, the background density and potential temperature distributions in (27) obey

$$(\overline{\hat{\rho}}, \overline{\hat{\theta}})(\hat{z}) = (\overline{\rho}, \overline{\theta})(z_0 + \delta\hat{z}) = (\overline{\rho}, \overline{\theta})(z_0) + O(\delta) \quad \text{for} \quad \hat{z} = O(1) \quad \text{as} \quad \delta \to 0. \tag{47}$$

In the limit, $(\overline{\hat{\rho}}, \overline{\hat{\theta}}) \equiv (\overline{\rho}, \overline{\theta})(z_0) = \text{const}$, and the anelastic model from (26) becomes identical to the **Boussinesq-approximation**

$$\begin{aligned} \nabla \cdot \boldsymbol{v} &= 0 \\ \boldsymbol{v}_t + \boldsymbol{v} \cdot \nabla \boldsymbol{v} + \nabla \pi' &= g\theta \boldsymbol{k} \\ \theta_t + \boldsymbol{v} \cdot \nabla \theta &= 0. \end{aligned} \tag{48}$$

Analogously, $\overline{P} \to \overline{P}(z_0)$ as $\delta \to 0$ in (35), and the pseudo-incompressible model from (41) reduces to the more general
Zero Mach, variable density flow equations

$$\begin{aligned} \rho_t + \nabla \cdot (\rho\boldsymbol{v}) &= 0 \\ (\rho\boldsymbol{v})_t + \nabla \cdot (\rho\boldsymbol{v} \circ \boldsymbol{v}) + \nabla \pi &= -g\rho \boldsymbol{k} \\ \nabla \cdot \boldsymbol{v} &= 0. \end{aligned} \tag{49}$$

To simplify the notation, we have absorbed a factor of $\overline{\theta}(z_0)$ in θ in (48), and a factor of $\overline{P}(z_0)$ in π in (49).

Both the Boussinesq approximation and the zero Mach number variable density flow equations do have systematic asymptotic derivations from the full compressible flow equations, see, e.g., [42,53,57]. The Boussinesq approximation is more restrictive as it requires small density variations in addition to vanishing Mach number. We conclude that, at least on small scales, there is asymptotic agreement of the anelastic and pseudo-incompressible models with the full compressible flow equations and that the pseudo-incompressible model is more general in that it is not restricted to small potential temperature variations.

This latter observation may be of interest in the context of high-resolution and LES models for meteorological applications. On length scales comparable to the pressure scale height, the differences between simulation results obtained with either sound-proof model differ only very little as discussed in Sect. 4.1. For simulations involving much smaller scales, the pseudo-incompressible model is preferable as it remains uniformly valid independent of the magnitude of density or potential temperature variations. A related example is given in Sect. 4.3.

3 Finite-volume sound-proof model solver

The scheme proposed in this section combines ideas from [5,10,24,41,43,55,56] as follows. Borrowing from the projection methods in [5,41], from the auxiliary variable projection approach in [24], and from the well-balanced discretizations for the gravity source term in [10], the scheme consists of

1. Predictor step, including
   (a) Godunov-type advection (Sect. 3.1.1)
   (b) Well-balanced discretization of the gravity term (Sect. 3.1.2)
2. MAC-projection (Marker and Cell) for the advective fluxes (Sect. 3.2)
3. Projection of the cell-centered velocity fields (Sect. 3.3)

Following [43], we assign a special role to the divergence-controlled fields $P\boldsymbol{v}$ (or $\rho\theta\boldsymbol{v}$) in the pseudo-incompressible model and $\rho\boldsymbol{v}$ in the anelastic model in that upwinding in the Godunov-type advection scheme is done relative to these fields. Thus, the advective flux $\rho\phi\boldsymbol{v}$ of some quantity ϕ is discretized in Sect. 3.1.1 as $(\rho\theta\boldsymbol{v})(\phi/\theta)^{\text{upw}}$ and $(\rho\boldsymbol{v})\phi^{\text{upw}}$, respectively, with $(\rho\theta\boldsymbol{v})$ and $(\rho\boldsymbol{v})$ obtained from upwind-free interpolations.

Following [10], we describe in Sect. 3.1.2 an explicit well-balanced discretization of the gravity source term based on local hydrostatic reconstruction and Archimedes' principle. This approach is used in [10] to discretize the compressible Euler equations for atmospheric applications without reference to a hydrostatically balanced background state, and we achieve the same here for the pseudo-incompressible and anelastic models (except, of course, for the explicit dependence of the buoyancy term on $\overline{\theta}$ in the anelastic model).

The MAC-projection described in Sect. 3.2 controls the divergence of the advection velocities in a some-what non-standard fashion. Consider first the approach for the pseudo-incompressible model. Rather than directly enforcing $\nabla \cdot (\overline{\rho\theta}\boldsymbol{v}) = 0$, which would require explicit evaluation of the background distribution $\overline{\rho\theta}(z)$, we enforce $\nabla \cdot (\rho\theta\boldsymbol{v}) = 0$ [without the overbar]. This will guarantee that, upon updating $\rho\theta$ to the new time level according to the potential temperature transport equation $(\rho\theta)_t + \nabla \cdot (\rho\theta\boldsymbol{v}) = 0$, the quantity $\rho\theta$ will retain its old time level and thus its distribution at the initial time, up to the tolerance to which the divergence constraint is enforced. As a consequence, we have $\nabla \cdot (\overline{\rho\theta}\boldsymbol{v}) = \nabla \cdot (\rho\theta\boldsymbol{v})$ + h.o.t. at the discrete level where h.o.t. denotes higher-order terms that do not affect the second-order accuracy of the scheme, and the pseudo-incompressible divergence constraint is satisfied. Note that we also solve a discrete version of the mass continuity equation, $\rho_t + \nabla \cdot (\rho\boldsymbol{v}) = 0$, for which, however, $\nabla \cdot (\rho\boldsymbol{v}) \not\equiv 0$, so that a non-trivial time evolution of the density distribution results. In fact, our analysis given in Appendix A1 below shows that the approach provides a second-order accurate discretization of the advection of $1/\theta$ independent of the tolerance with which we control the divergence of $\rho\theta\boldsymbol{v}$.

For the anelastic model, the variables $\rho\theta$ and ρ switch their roles, with $\nabla \cdot \rho\boldsymbol{v}$ being controlled and the equation $(\rho\theta)_t + \nabla \cdot (\rho\theta\boldsymbol{v}) = 0$ being responsible for the advection of θ.

The same strategy is applied in the final projection of the cell-centered velocities described in Sect. 3.3. This "second projection" is a derivative of the inf-sup-stable projection for the zero-Froude number shallow water equations developed in [55,56].

The entire scheme accesses the background distributions only within the formulations of initial and boundary conditions and, as mentioned above, in the gravity term for the anelastic model.

3.1 Predictor

In the predictor step, we solve the following auxiliary hyperbolic systems using Godunov-type upwind techniques:

Auxiliary system

$$\rho_t + \nabla \cdot (\rho\boldsymbol{v}) = 0$$
$$(\rho\boldsymbol{v})_t + \nabla \cdot (\rho\boldsymbol{v} \circ \boldsymbol{v}) + \rho\chi\nabla\pi^n = -g\rho\Theta\boldsymbol{k} \tag{50}$$
$$(\rho\theta)_t + \nabla \cdot (\rho\theta\boldsymbol{v}) = 0.$$

Here π^n is the approximate Exner pressure field from the respective last completed, i.e., nth, time level, and

$$(\chi, \Theta) = \begin{cases} (\theta, 1) & \text{pseudo-inc.} \\ \left(1, \left[1 - \frac{\theta-\bar{\theta}}{\bar{\theta}}\right]\right) & \text{anelastic} \end{cases} \tag{51}$$

As in [43], we cast the individual equations in these auxiliary systems into the generic form

$$(\hat{\rho}\phi)_t + \nabla \cdot (\hat{\rho}\phi\boldsymbol{v}) + \hat{\rho}Q^\phi = 0, \tag{52}$$

where

$$\begin{aligned} \hat{\rho} = \rho\theta, \phi \in \{1/\theta, u/\theta, w/\theta, 1\} & \quad \text{pseudo-inc.} \\ \hat{\rho} = \rho, \phi \in \{1, u, w, \theta\} & \quad \text{anelastic} \end{aligned} \tag{53}$$

and u and w are cartesian velocity components. The additional term Q^ϕ is non-zero only for the momentum equations with

$$Q^\phi = \begin{cases} 0 & (\phi \in \{1/\chi, \theta/\chi\}) \\ \partial\pi^n/\partial x & (\phi = u/\chi) \\ \partial\pi^n/\partial z + g\Theta/\chi & (\phi = w/\chi) \end{cases}. \tag{54}$$

Second-order predictions for these auxiliary systems provide second-order accurate advective fluxes for the full pseudo-incompressible and anelastic systems. See the analogous discussions in [24,41]. In Sect. 3.1.1, we describe the discretization of the advective transport terms, in Sect. 3.1.2 we address Q^ϕ.

Notation For the predictor step, we use Strang-splitting for the spatial directions on an equally spaced cartesian mesh. In describing the scheme, we use the generic notation

$$
\begin{aligned}
x &: \text{current computational direction} \\
u &: \text{flow velocity in the } x\text{-direction} \\
i &: \text{grid cell index} \\
g &: \text{gravitational acceleration if } x\text{-direction is vertical, 0 otherwise}
\end{aligned}
$$

3.1.1 MUSCL scheme for advection

We use a slightly modified MUSCL-approach (Monotone Upstream Scheme for Conservation Laws) to discretize the advection terms (see, e.g., [35,54] and references therein). The generic update for the one-dimensional advection step reads

$$
(\hat{\rho}\phi)_i^{n+1} = (\hat{\rho}\phi)_i^n - \lambda \left((\hat{\rho}u\phi)_{i+\frac{1}{2}}^{n+\frac{1}{2}} - (\hat{\rho}u\phi)_{i-\frac{1}{2}}^{n+\frac{1}{2}} \right) - \Delta t\, Q_i^{\phi,n+\frac{1}{2}}, \tag{55}
$$

with $\lambda = \frac{\Delta t}{\Delta x}$ and the numerical fluxes $(\hat{\rho}u\phi)_{i+\frac{1}{2}}^{n+\frac{1}{2}}$ computed as follows: first, we determine left and right cell-edge data for ϕ via

$$
\begin{aligned}
\phi_{i+\frac{1}{2}}^{n+\frac{1}{2},-} &= \phi_i^n + \frac{\Delta x}{2} \left(1 - \lambda u_i^n\right) s_i^{n,+} - \frac{\Delta t}{2} Q_{i+\frac{1}{2}}^{\phi,n} \\
\phi_{i+\frac{1}{2}}^{n+\frac{1}{2},+} &= \phi_{i+1}^n - \frac{\Delta x}{2} \left(1 + \lambda u_{i+1}^n\right) s_{i+1}^{n,-} - \frac{\Delta t}{2} Q_{i+\frac{1}{2}}^{\phi,n}.
\end{aligned} \tag{56}
$$

(See Sect. 3.1.2 for the discretizations of $Q_i^{\phi,n+\frac{1}{2}}$ and $Q_{i+\frac{1}{2}}^{\phi,n}$ from (55), (56), respectively).

In (56) the

$$
s_i^{n,\pm} = \pm\mathrm{sgn}\left(\phi_{i\pm1}^n - \phi_i^n\right) \left(\partial_x^{\lim}\phi\right)_i^n, \quad \left(\partial_x^{\lim}\phi\right)_i^n = \mathrm{Lim}\left(\left| \frac{\phi_i^n - \phi_{i-1}^n}{\Delta x} \right|, \left| \frac{\phi_{i+1}^n - \phi_i^n}{\Delta x} \right| \right) \tag{57}
$$

are limited slopes. In producing the results presented in Sect. 4, we have used variations of van Leer's limiter,

$$
\mathrm{Lim}(a,b) = \begin{cases} \dfrac{2ab}{a+b}\, \psi\left(\min(a/b, b/a)\right) & (\mathrm{sgn}(ab) > 0) \\ 0 & \text{otherwise} \end{cases}, \quad \psi(r) = 1 + r(1-r)(1-r^k). \tag{58}
$$

For $k = 0$, $\psi \equiv 1$ and we recover van Leer's original limiter. For $k = 1, 2, 3, 4$ the limiter function remains smooth but "sharpens" in that its ability to maintain steep gradients improves. We have introduced this modified limiter, because smooth limiter functions that are free of "if–then" decisions provide for superior maintainance of flow symmetries in comparison with limiters that are not. (See Appendix A2 for further discussion).

The formulae in (57) are non-standard in that we distinguish a left and a right linear reconstruction in each cell. Wherever $\left(\phi_{i+1}^n - \phi_i^n\right)\left(\phi_i^n - \phi_{i-1}^n\right) \geq 0$, we have $s_i^{n,+} = s_i^{n,-}$ and the reconstruction is equivalent to that of a standard MUSCL-scheme. At an extremum, however, slopes are not set to zero as they normally would be. Instead a limited slope is computed from the modulus of the discrete left and right slopes, and left and right reconstructions are distinguished within the cell. This modification led to considerably reduced damping in the strongly flucutating flows induced by gravity wave breaking in one of the tests discussed below.

See Appendix A3 for a variant of the present scheme that uses standard TVD slope limiting and is shown to observe a maximum principle.

For the density variable $\hat{\rho}$ whose overall evolution, including the influence of the marker-and-cell (MAC)-projection, is controlled by the divergence constraint, we use central differencing in the half-time update, i.e.,

$$
\hat{\rho}_{i+\frac{1}{2}}^{n+\frac{1}{2}} = \frac{1}{2}\left(\hat{\rho}_i^n + \hat{\rho}_{i+1}^n\right) - \frac{\Delta t}{2\Delta x}\left((\hat{\rho}u)_{i+1}^n - (\hat{\rho}u)_i^n\right). \tag{59}
$$

With these ingredients, we compute the advective numerical flux for ϕ from

$$
\begin{aligned}
(\hat{\rho} u \phi)_{i+\frac{1}{2}}^{n+\frac{1}{2}} &= \left(\hat{\rho} \langle u \rangle \phi^{\text{upw}}\right)_{i+\frac{1}{2}}^{n+\frac{1}{2}}, \\
\langle u \rangle_{i+\frac{1}{2}}^{n+\frac{1}{2}} &= \frac{1}{2}\left(u_{i+\frac{1}{2}}^{n+\frac{1}{2},+} + u_{i+\frac{1}{2}}^{n+\frac{1}{2},-}\right),
\end{aligned}
\tag{60}
$$

where

$$
\phi^{\text{upw}} = \sigma \, \phi^{+} + (1-\sigma) \, \phi^{-}, \quad \sigma = \frac{1}{2}(1 - \text{sgn}\langle u \rangle)
\tag{61}
$$

is the upwind value of ϕ based on the averaged advection velocity $\langle u \rangle$.

3.1.2 Well-balanced discretization of the pressure gradient and gravity terms

We need to evaluate the pressure gradient and gravity terms in two places in the scheme: (1) to produce the half-time update of the cell-interface fluxes in (56), and (2) for the update of the cell-averaged momenta in (55). As in [10], we adopt Archimedes' principle and represent the gravity term by the gradient of a locally reconstructed hydrostatic pressure.

Cell interfaces

The cell-interface half-time updates in (55) are $Q_{i+\frac{1}{2}}^{\phi,n} = 0$ for $\phi \neq u$ and

$$
Q_{i+\frac{1}{2}}^{u,n} = \left(\frac{\partial \pi^n}{\partial x} + g \frac{\Theta}{\chi}\right)_{i+\frac{1}{2}}^{n} = \left(\frac{\pi_{i+1}^n - \pi_i^n}{\Delta x} - \frac{\pi_i^{h,n}(x_{i+1}) - \pi_i^{h,n}(x_i)}{\Delta x}\right),
\tag{62}
$$

with the local hydrostatic pressure distributions

$$
\pi_i^{h,n}(x) = \pi_i^n - \int_{x_i}^{x} g\left(\frac{\Theta}{\chi}\right)(\zeta) \, d\zeta.
\tag{63}
$$

The integral is evaluated analytically using piecewise linear interpolation for Θ/χ, i.e.,

$$
\left(\frac{\Theta}{\chi}\right)(x) = \left(\frac{\Theta}{\chi}\right)_i^n + (x - x_i)\frac{(\Theta/\chi)_{i+1}^n - (\Theta/\chi)_i^n}{\Delta x} \quad \text{for} \quad (x_i \le x < x_{i+1}).
\tag{64}
$$

These formulae hold for all cartesian directions with g assuming its standard value for the vertical direction and zero for the horizontal ones.

Cell centers

The updates of the momentum cell averages read

$$
(\rho u)_i^{n+1,*} = (\rho u)_i^n - \lambda \left(\left(\hat{\rho} \langle u \rangle u^{\text{upw}}\right)_{i+\frac{1}{2}}^{n+\frac{1}{2}} - \left(\hat{\rho} \langle u \rangle u^{\text{upw}}\right)_{i-\frac{1}{2}}^{n+\frac{1}{2}}\right) - \Delta t \left(\hat{\rho}\left[\frac{\partial \pi^n}{\partial x} + g \frac{\Theta}{\chi}\right]\right)_i^{n+\frac{1}{2}},
\tag{65}
$$

with

$$
\left(\hat{\rho}\left[\frac{\partial \pi^n}{\partial x} + g \frac{\Theta}{\chi}\right]\right)_i^{n+\frac{1}{2}} = \hat{\rho}_i^{n+\frac{1}{2}}\left(\frac{1}{2}\left[Q_{i-\frac{1}{2}}^{u,n} + Q_{i+\frac{1}{2}}^{u,n}\right] + \frac{g \Delta t}{2}\left(\frac{\partial}{\partial t}\frac{\Theta}{\chi}\right)_i^n\right).
\tag{66}
$$

Here the $Q_{i-\frac{1}{2}}^{u,n}$ are taken from (62), and the last term in (66) provides the half-time update of the gravity term needed to ensure a second-order accurate approximation. For this last term, we have

$$
\hat{\rho}_i^{n+\frac{1}{2}} = \frac{1}{2}\left(\hat{\rho}_{i+\frac{1}{2}}^{n+\frac{1}{2}} + \hat{\rho}_{i-\frac{1}{2}}^{n+\frac{1}{2}}\right),
\tag{67}
$$

and, recalling the definitions of Θ and χ in (51) and that $1/\theta$ and θ are advected quantities in the pseudo-incompressible and anelastic models, respectively, we let

$$\left(\frac{\partial}{\partial t}\frac{\Theta}{\chi}\right)^n_i = \begin{cases} -\frac{u^n_i}{2\Delta x}\left((1/\theta)^n_{i+1} - (1/\theta)^n_{i-1}\right) & \text{pseudo-inc.} \\[2ex] \frac{u^n_i}{2\Delta x \bar{\theta}(x_i)}\left(\theta^n_{i+1} - \theta^n_{i-1}\right) & \text{anelastic} \end{cases}. \tag{68}$$

Instead of central differences we have also tested limited slopes in this term. The differences are small (not shown).

3.2 Marker and cell (MAC) projection of the advective fluxes

The projection steps are inherently multi-dimensional, and we describe here the implementation for two space dimensions, dropping the simplified dimensionally split notation of the last section.

The predictor step produces a preliminary advective update for $\hat{\rho}$ through

$$\hat{\rho}^{n+1,*}_{i,j} - \hat{\rho}^n_{i,j} = -\Delta t \left(\tilde{\nabla}\cdot\hat{\rho}\boldsymbol{v}\right)^{n+\frac{1}{2},*}_{i,j}, \tag{69}$$

where the right-hand side represents the accumulated discrete finite volume flux divergence over a full Strang-splitting cycle for the cartesian directions. This flux divergence will be non-zero in general because the auxiliary equation in (50) involves the old time level pressure gradient in the momentum equation instead of a pressure field adjusted so as to enforce the divergence constraint on the flux of $\hat{\rho}$. Also, this use of the old time level pressure is the only source of error that prevents the predictor step from attaining the desired second-order accuracy. Therefore, in the MAC-projection step we compute a pressure correction π' whose gradient adjusts the flux of $\hat{\rho}$ to comply with the divergence constraint. Specifically, we let, e.g., for the x-direction,

$$(\hat{\rho}u)^{n+\frac{1}{2}}_{i+\frac{1}{2},j} = (\hat{\rho}u)^{n+\frac{1}{2},*}_{i+\frac{1}{2},j} - \frac{\Delta t}{2}\left(\hat{\rho}\chi\frac{\partial\pi'}{\partial x}\right)^{n+\frac{1}{2}}_{i+\frac{1}{2},j}. \tag{70}$$

Inserting this into (69), we obtain a Poisson-type equation for π',

$$\frac{1}{\hat{\rho}^{n+1,*}_{i,j}}\left(\tilde{\nabla}\cdot(\hat{\rho}\chi\tilde{\nabla}\pi')\right)^{n+\frac{1}{2}}_{i,j} = \frac{2}{(\Delta t)^2}\frac{\hat{\rho}^{n+1,*}_{i,j} - \hat{\rho}^n_{i,j}}{\hat{\rho}^{n+1,*}_{i,j}}. \tag{71}$$

The scaling by $1/\hat{\rho}$ represents a diagonal preconditioner that ensures accurate corrections of the advection velocities even for deep atmospheres in which $\hat{\rho}$ varies vertically by several orders of magnitude.

For the discrete divergence, $\tilde{\nabla}\cdot$, in (71) we use the standard finite volume flux divergence. To approximate the required integral of $\hat{\rho}\chi\nabla\pi'\cdot\boldsymbol{n}$ over the grid cell interfaces, we adopt the discretization from [51,55]. Specifically, we assume piecewise bilinear continuous ansatz functions for π' on the dual cells of the cartesian mesh and piecewise constant data for $\hat{\rho}\chi$ on the interfaces of the primary cells. Then, we approximate the discrete divergence by exact integrations along the boundaries of the primary cells. The resulting discrete weighted Laplacian is composed of flux contributions across the grid cell interfaces, so that

$$\tilde{\nabla}\cdot(\hat{\rho}\,\chi\,\tilde{\nabla}\pi')_{i,j} = \frac{1}{\Delta x}\left(F^{\text{MAC}}_{i+\frac{1}{2},j} - F^{\text{MAC}}_{i-\frac{1}{2},j}\right) + \frac{1}{\Delta z}\left(G^{\text{MAC}}_{i,j+\frac{1}{2}} - G^{\text{MAC}}_{i,j-\frac{1}{2}}\right), \tag{72}$$

with

$$\begin{aligned} F^{\text{MAC}}_{i+\frac{1}{2},j} &= (\hat{\rho}\chi)^{n+\frac{1}{2},*}_{i+\frac{1}{2},j}\left(\frac{3}{4}\frac{\pi'_{i+1,j} - \pi'_{i,j}}{\Delta x} + \frac{1}{8}\left[\frac{\pi'_{i+1,j+1} - \pi'_{i,j+1}}{\Delta x} + \frac{\pi'_{i+1,j-1} - \pi'_{i,j-1}}{\Delta x}\right]\right) \\ (\hat{\rho}\chi)^{n+\frac{1}{2},*}_{i+\frac{1}{2},j} &= \frac{1}{4}\left(\left[(\hat{\rho}\chi)^{n+\frac{1}{2},*}_{i,j} + (\hat{\rho}\chi)^n_{i,j}\right] + \left[(\hat{\rho}\chi)^{n+\frac{1}{2},*}_{i+1,j} + (\hat{\rho}\chi)^n_{i+1,j}\right]\right), \end{aligned} \tag{73}$$

and analogous formulae for $G^{\text{MAC}}_{i,j+\frac{1}{2}}$.

Having solved for π', we correct the predictions for advected quantities by

$$
\begin{aligned}
(\hat{\rho}\phi)_{i,j}^{n+1} = {}& (\hat{\rho}\phi)_{i,j}^{n+1,*} \\
& + \frac{(\Delta t)^2}{2} \left\{ \frac{(\phi F)_{i+\frac{1}{2},j}^{\text{MAC}} - (\phi F)_{i-\frac{1}{2},j}^{\text{MAC}}}{\Delta x} + \frac{(\phi G)_{i,j+\frac{1}{2}}^{\text{MAC}} - (\phi G)_{i,j-\frac{1}{2}}^{\text{MAC}}}{\Delta z} \right\} - \frac{\Delta t}{2} \hat{\rho} Q'^{\phi}_{i,j}
\end{aligned} \tag{74}
$$

with

$$
\begin{aligned}
(\phi F)_{i+\frac{1}{2},j}^{\text{MAC}} &= \phi_{i+\frac{1}{2},j}^{\text{upw}} F_{i+\frac{1}{2},j}^{\text{MAC}} \\
\phi_{i+\frac{1}{2},j}^{\text{upw}} &= \sigma \phi_{i-1,j}^{n+1,*} + (1-\sigma)\phi_{i,j}^{n+1,*} \\
\sigma &= \text{sgn}\left((\hat{\rho}u)_{i+\frac{1}{2},j}^{n+\frac{1}{2},*} - \frac{\Delta t}{2} F_{i+\frac{1}{2},j}^{\text{MAC}} \right),
\end{aligned} \tag{75}
$$

analogous formulae for $(\phi G)_{i,j+\frac{1}{2}}^{\text{MAC}}$, and

$$
\hat{\rho} Q'^{\phi}_{i,j} = \begin{cases} \frac{1}{2}\left(F_{i-\frac{1}{2},j}^{\text{MAC}} + F_{i+\frac{1}{2},j}^{\text{MAC}} \right) & (\phi = u/\chi) \\[2mm] \frac{1}{2}\left(G_{i,j-\frac{1}{2}}^{\text{MAC}} + G_{i,j+\frac{1}{2}}^{\text{MAC}} \right) & (\phi = w/\chi) \\[2mm] 0 & \text{otherwise} \end{cases} \tag{76}
$$

Remarks In (75)$_2$, we have also tried more involved second-order central and third-order upwind-biased interpolations. The effects are small, they do not affect second-order accuracy of the scheme, and the simple upwinding formula has the advantage of obeying the maximum principle for advected scalars as shown in Appendix A3. Thus, the simple first-order upwind formula is sufficient and has been used in all computations presented in this paper.

Updating the cell-averaged momenta by $Q'^{u/\chi}_{i,j}$ and $Q'^{v/\chi}_{i,j}$ from (76) acts as a preconditioner for the second projection step described in the next section. Although not sufficient to ensure second-order accuracy of the momentum updates or to reduce the flow divergence to truncation errors less than $O((\Delta x)^2)$, these preliminary updates do result from elliptic pressure corrections that ensure the divergence constraint on the mass- and $\rho\theta$ fluxes, thereby containing valid information on the pressure field. We found that using these updates reduces the number of CG-iterations needed to achieve a given tolerance in the second projection for the cell-centered velocities by more than one half on average.

3.3 Projection of the cell-centered velocities

The cell-averaged momenta have been updated in the predictor taking into account second-order accurate advection but only first-order accurate pressure gradient terms. As in [5,41], we introduce a second node- or dual-cell-centered projection to achieve second-order accuracy. We use again the discretization of the weighted Poisson operator from [56]. For simplicity, we do not implement the exact projection version described in [56], which would imply monitoring and correcting the slopes of the momenta within the grid cells in addition to correcting their cell averages. Thus, here we introduce an approximate projection for the cell-centered velocities similar to those analyzed in [3]. Note, however, that the advective fluxes are exactly projected, as described in the previous section.

We determine the predicted discrete flow divergence for dual cells through, dropping the $(\cdot)^{n+1,*}$-superscript,

$$
\begin{aligned}
(\tilde{\nabla}\cdot(\hat{\rho}\boldsymbol{v}))_{i+\frac{1}{2},j+\frac{1}{2}} = {}& \frac{1}{2\Delta x} \left(\left[(\hat{\rho}u)_{i+1,j+1} + (\hat{\rho}u)_{i+1,j} \right] - \left[(\hat{\rho}u)_{i,j+1} + (\hat{\rho}u)_{i,j} \right] \right) \\
& + \frac{1}{2\Delta z} \left(\left[(\hat{\rho}w)_{i+1,j+1} + (\hat{\rho}w)_{i,j+1} \right] - \left[(\hat{\rho}w)_{i+1,j} + (\hat{\rho}w)_{i,j} \right] \right).
\end{aligned} \tag{77}
$$

To achieve approximately divergence-free fields $\hat{\rho}\boldsymbol{v}$, we correct the momenta by the approximate gradient of a node-based pressure field, $\pi'_{i+\frac{1}{2},j+\frac{1}{2}}$, so that

$$(\rho u)_{i,j}^{n+1} = (\rho u)_{i,j}^{n+1,*} - \frac{\Delta t}{2\Delta x}(\hat{\rho}\chi)_{i,j}^{n+1}\left(\left[\pi'_{i+\frac{1}{2},j+\frac{1}{2}} + \pi'_{i+\frac{1}{2},j-\frac{1}{2}}\right] - \left[\pi'_{i-\frac{1}{2},j+\frac{1}{2}} + \pi'_{i-\frac{1}{2},j-\frac{1}{2}}\right]\right), \quad (78)$$

with an analogous formula for ρw.

The pressure field satisfies the (preconditioned) Poisson-type equation

$$\frac{1}{\hat{\rho}}\tilde{\nabla} \cdot (\hat{\rho}\chi\tilde{\nabla}\pi')_{i+\frac{1}{2},j+\frac{1}{2}} = \frac{1}{\Delta t}\left(\frac{1}{\hat{\rho}}\tilde{\nabla} \cdot (\hat{\rho}\boldsymbol{v})\right)_{i+\frac{1}{2},j+\frac{1}{2}}, \quad (79)$$

where

$$\tilde{\nabla} \cdot (\hat{\rho}\chi\tilde{\nabla}\pi')_{i+\frac{1}{2},j+\frac{1}{2}} = \frac{1}{\Delta x}\left(F^{\text{sp}}_{i+1,j+\frac{1}{2}} - F^{\text{sp}}_{i,j+\frac{1}{2}}\right) + \frac{1}{\Delta z}\left(G^{\text{sp}}_{i+\frac{1}{2},j+1} - G^{\text{sp}}_{i+\frac{1}{2},j}\right), \quad (80)$$

with

$$\begin{aligned}
F^{\text{sp}}_{i+1,j+\frac{1}{2}} = {}& \frac{1}{2}((\hat{\rho}\chi)_{i+1,j} + (\hat{\rho}\chi)_{i+1,j+1})\frac{3}{4\Delta x}\left(\pi'_{i+\frac{3}{2},j+\frac{1}{2}} - \pi'_{i+\frac{1}{2},j+\frac{1}{2}}\right) \\
& + \frac{1}{8\Delta x}\left((\hat{\rho}\chi)_{i+1,j+1}^{n+1}\left(\pi'_{i+\frac{3}{2},j+\frac{3}{2}} - \pi'_{i+\frac{1}{2},j+\frac{3}{2}}\right)\right) \\
& + \frac{1}{8\Delta x}\left((\hat{\rho}\chi)_{i+1,j}^{n+1}\left(\pi'_{i+\frac{3}{2},j-\frac{1}{2}} - \pi'_{i+\frac{1}{2},j-\frac{1}{2}}\right)\right)
\end{aligned} \quad (81)$$

and the analogous definition for $G^{\text{sp}}_{i+\frac{1}{2},j+1}$.

The elliptic equations defined in this section have all been solved by either a matrix-free implementation of the classical BiCGStab method, or by a conjugate residual scheme as described by Smolarkiewicz and Margolin in [45].

4 Properties of the flow models and the numerical scheme and related tests

This section provides empirical evidence that the scheme proposed above

- Captures convective motions as well as (nonlinear) internal waves,
- Produces nearly the same results when used to solve either the anelastic or the pseudo-incompressible model equations for flows with characteristic scales comparable to the pressure scale height and larger, thereby corroborating findings by Smolarkiewicz and Dörnbrack, [43],
- Reveals the expected differences between the models for flows on smaller scales with large potential temperature variations,
- Is robust with respect to large tolerances in the stopping criteria for the CG-iterations in the projection steps.

We will also demonstrate that the differences in the results produced by varying the numerical scheme within the range of second-order methods are larger than the differences obtained when switching between the anelastic and pseudo-incompressible model but using the same numerics components. This, too, supports the findings in [43].

4.1 Breaking lee waves: influences of flow model, divergence tolerance, and nonlinear slope limiting

4.1.1 Description of the test case, (from Smolarkiewicz and Margolin, [46])

In a domain of dimensions -60 km $\leq x \leq 60$ km and $z_0(x) \leq z \leq 60$ km, we embed a stably stratified atmosphere with constant Brunt-Väisälä frequency of $N = 0.01$ s^{-1}. There is a constant barotropic background wind sweeping from left to right (from $x < 0$ to $x > 0$) at 10 m/s over the "witch of Agnesi" bottom topography

$$z_0(x) = \frac{z_\infty}{1 + (x/\ell)^2}, \quad \begin{array}{l} z_\infty = 2\pi \times 100 \text{ m} \\ \ell = 1 \text{ km} \end{array}. \tag{82}$$

The hydrostatic density distribution is computed assuming an ideal gas with constant specific heat capacities and an isentropic exponent of $\gamma = 1.0696864111498257$, a base density at $z = 0$ of 1 kg/m^3, and a gravitational acceleration of $g = 10$ m/s^2. The "weird" value of the isentropic exponent is chosen such that the potential temperature as well as the hydrostatic density and pressure distributions are all exponential. For the same potential temperature distribution with constant buoyancy frequency but larger, more realistic values of the isentropic exponent, pressure and density would drop to zero at heights less than 60 km, and the test case would be meaningless.

The bottom boundary condition is implemented approximately in that we impose a vertical velocity at the flat bottom boundary that equals the horizontal velocity in the adjacent grid cell times the slope of the topography.

The rigid wall boundary conditions at the top and bottom of the domain and periodic conditions in the horizontal are combined with damping/driving layers near the left, right, and top boundaries. In these layers, the solution is relaxed towards the hydrostatic background state and mean wind. This relaxation is implemented by incorporating source terms for (u, w, θ) in either model through two additional Strang splitting steps directly before and after the predictor step from Sect. 3.1, which enforce

$$\phi^{\text{new}} = \phi^{\text{bg}} + \frac{\phi^{\text{old}} - \phi^{\text{bg}}}{1 + \alpha \Delta t/2}, \quad (\phi \in \{u, w, \theta\}), \tag{83}$$

where ϕ^{bg} is the prescribed background state. This corresponds to two half-time steps for the relaxation equation $d\phi/dt = -\alpha(\phi - \phi^{\text{bg}})$ discretized by the backward first-order Euler scheme. The relaxation rate, α, is

$$\alpha(x, z) = \max(\alpha_l(x), \alpha_r(x), \alpha_t(z)) \quad \text{where} \quad \begin{cases} \alpha_l(x) = \max(0, \alpha_x(x - x_l)/D_x) \\ \alpha_r(x) = \max(0, \alpha_x(x_r - x)/D_x) \\ \alpha_t(z) = \max(0, \alpha_z(z_t - z)/D_z) \end{cases} \tag{84}$$

with

$$\alpha_x = \alpha_z = \frac{1}{600 \text{ s}}, \quad D_x = D_z = 20 \text{ km}. \tag{85}$$

We have also experimented with $\alpha_x = 1/120$ s, $D_x = 5$ km but found little difference in the essential characteristics of the solutions.

In all computations for the breaking wave tests the time step is determined by

$$\Delta t = \min(31 \text{ s}, \text{CFL} \Delta x / \max_\Omega(|u|, |w|)) \quad \text{with} \quad \text{CFL} = 1.0 \tag{86}$$

where $\max_\Omega(|u|, |w|)$ denotes the maximum over the flow domain of the horizontal and vertical velocities.

This test was suggested to us by P. Smolarkiewicz [46].

4.1.2 Results

Results for this test case sensitively depend on the dissipative properties of the considered scheme as explained in [46]. Following linear theory, one should expect wave breaking to have fully affected the upper downstream quarter of the domain some time between 3 and 4 h into the simulation. Smolarkiewicz and Margolin observe that the actual time of breaking depends on the numerical scheme used. A semi-Lagrangian version of their numerical scheme yielded wave breaking between 3 and 3.5 h, their Eulerian scheme, using the monotone positive definite advection transport algorithm (MPDATA), exhibited wave breaking between 2.5 and 3 h.

Figure 1a, b show contours of the potential temperature after 2.5 and 3 h into the simulation, obtained solving Durran's model with the scheme from Sect. 3 on a grid with 240×120 cells, controlling the divergence so that $\Delta t \nabla \cdot (\overline{P} \boldsymbol{v})/\overline{P} < \text{TOL}_{\text{div}} = 1.0 \times 10^{-3}$. This is our reference solution for the present test case. Its grid resolution matches that of the reference solution in [46] and it corresponds roughly to the minimal resolution necessary to obtain qualitatively correct behavior of the solution.
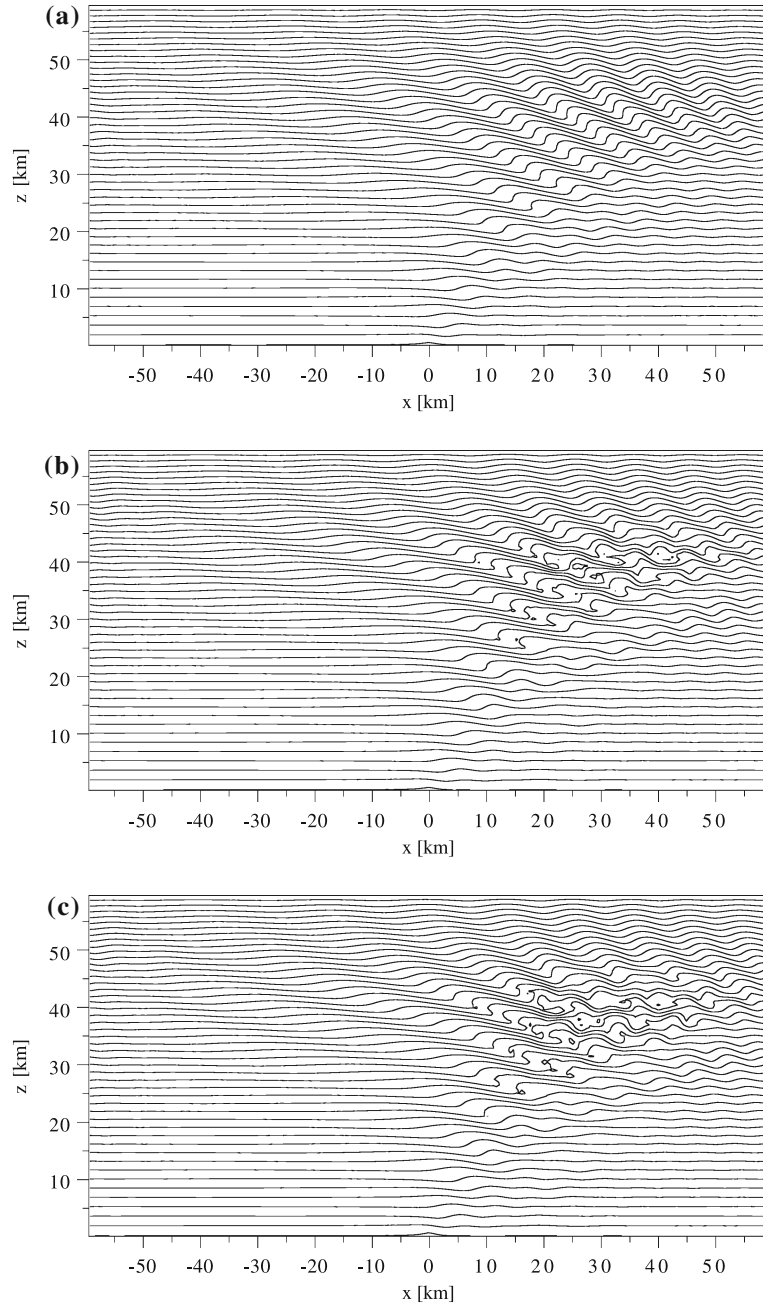
Fig. 1 Contours of potential temperature for the breaking wave test case from Sect. 4.1.1. **a** Pseudo-incompressible model, 2.5 h, **b** pseudo-incompressible model 3 h, **c** anelastic model, 3 h. Parameters of the numerical solution: 240×120 cells, sharpened van Leer's limiter, divergence tolerance 1.0×10^{-3}

Wave breaking occurs shortly after $t = 2.5$ h, indicating that the present scheme's numerical dissipation is comparable to that of MPDATA for this test case. After wave breaking, the numerical solution will strongly depend on the details of the numerical scheme, as localized small-scale instabilities arise and are captured by the scheme's nonlinear, local dissipation mechanism. The behavior of the present scheme after wave breaking is roughly comparable to the Eulerian version of MPDATA in [46].

Influence of the flow model. For the results in Fig. 1c we have used the exact same parameter setting as for Fig. 1a, b except that we have now solved the Bannon's anelastic model instead of the pseudo-incompressible
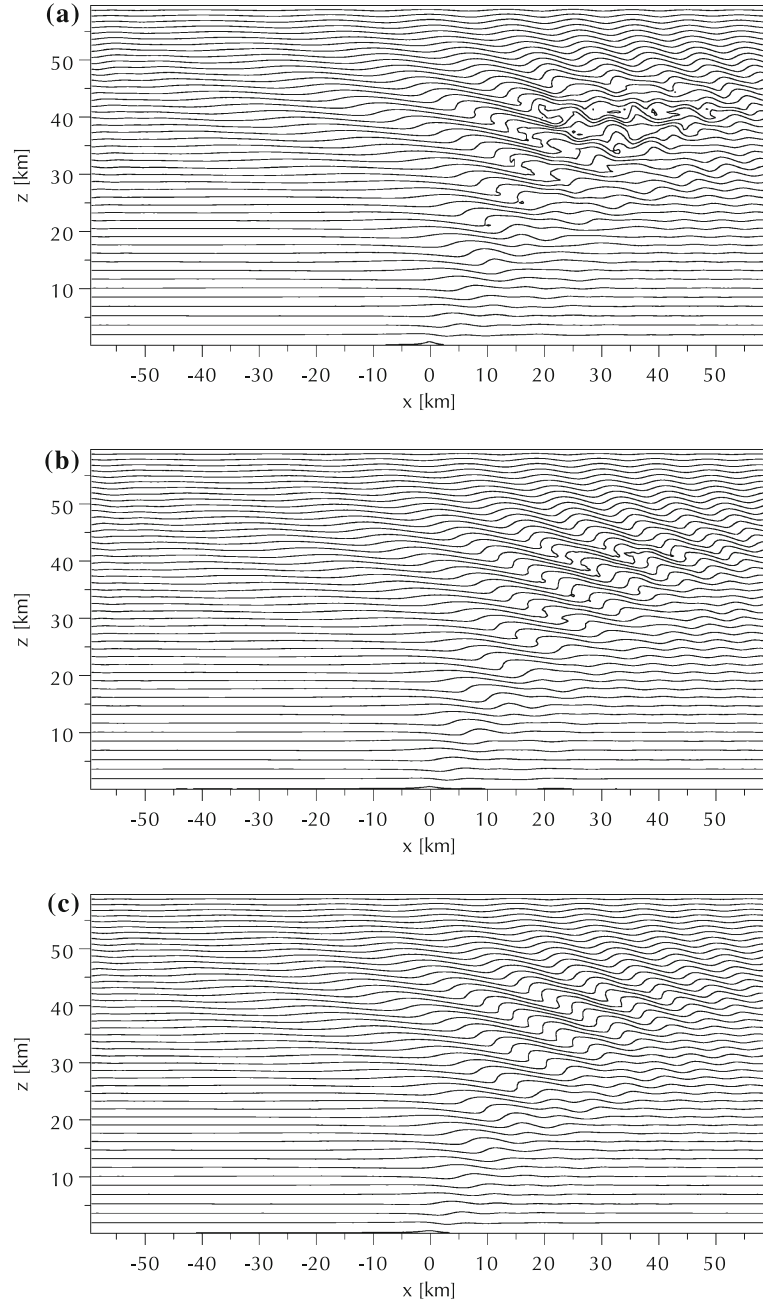
Fig. 2 Same as Fig. 1b but with divergence tolerances 1.0×10^{-6} (**a**) and 1.0×10^{-2} (**b**), and using the standard van Leer's limiter (**c**)

flow equations. Up to the time of wave breaking, the contours are practically identical, and the qualitative behavior after breaking is entirely comparable. This supports observations by Smolarkiewicz and Dörnbrack [43] who also find that the differences between computations based on the anelastic and pseudo-incompressible model equations for this test case are very small.

Influence of divergence tolerance. In Fig. 2a, we show results for the same test case, again with Durran's model and the same parameter set as for Fig. 1b, yet with a much tighter divergence control of $\text{TOL}_{\text{div}} = 1.0 \times 10^{-6}$. Again, the results differ only slightly from those shown in the earlier figures. We begin to see stronger deviations if instead of tightening, we loosen the divergence constraint. For Fig. 2b, we have used $\text{TOL}_{\text{div}} < 1.0 \times 10^{-2}$

and now the solution is considerably affected, although still qualitatively correct. Wave steepening is weaker, occuring 10–15 min later, and breaking is less violent.

In this last run with $\text{TOL}_{\text{div}} < 1.0 \times 10^{-2}$, the first projection step needed on average less than five conjugate residual or BICGSTAB iterations to achieve the required divergence control, the second iteration needed less than two iterations. We conclude that the pressure field will no longer be accurate in this setting with the said consequences for the overall solution. For completeness, with divergence tolerance $\text{TOL}_{\text{div}} = 1.0 \times 10^{-3}$, the first and second projections needed less than 10 and less than 4 iterations, respectively, while for $\text{TOL}_{\text{div}} = 1.0 \times 10^{-6}$ the iteration counts increased to roughly 120 and 65 for the first and second projections. Iteration counts were roughly the same, independently of whether we solved the anelastic or the pseudo-incompressible model equations.

Influence of the slope limiter. In the last paragraph we see how, for the breaking wave test problem, differences between simulations based on different model equations (anelastic vs. pseudo-incompressible) are small. Smaller, in particular, than the differences we see when solving one and the same model equation set with different levels of divergence control. Here, we show that comparable effects arise with variations of the slope limiting procedure, which represents a degree of freedom of the present second-order upwind technology.

In (58), we described the slope limiting procedure that is needed to avoid unphysical oscillations in the vicinity of sharp transients. If we insert $\psi(r) \equiv 1$ instead of $(58)_2$, we have van Leer's standard limiter function, and obtain the breaking wave test results displayed in Fig. 2c. Again, wave steepening is slowed down, wave breaking is delayed by about 15 min, and the structures after wave breaking are less violently fluctuating than in the reference case from Fig. 1b. The deviations between this run and the reference case are as large as those between the two runs with divergence tolerances $\text{TOL}_{\text{div}} = 1.0 \times 10^{-3}$ (Fig. 1b) and $\text{TOL}_{\text{div}} = 1.0 \times 10^{-2}$ (Fig. 2b), respectively.

This is somewhat disappointing, because the choice of the limiter function represents "just" a degree of freedom in the design of the second-order scheme, but it neither affects the scheme's fundamental design nor its order of convergence. One would therefore expect that the choice of a limiter function should not have a significant effect, yet it does. Nevertheless, with the "sharpened van Leer's limiter" from (58), we do obtain competetive results for the breaking wave test.

4.2 Rising hot plume: clipping of extrema

4.2.1 Description of the test case

In a box with rigid walls of dimensions $-10 \text{ km} \leq x \leq 10 \text{ km}$ and $0 \text{ km} \leq z \leq 10 \text{ km}$, we embed a neutrally stratified atmosphere that is at rest initially and perturbed by a bubble of hot air. We consider the following smoothed version of the cone-shaped initial distributions of potential temperature from [34],

$$\theta(0, x, z) = 300 \text{ K} + \begin{cases} \delta\theta \, \cos^2(\frac{\pi}{2}r) & (r \leq 1) \\ 0 & \text{otherwise} \end{cases}, \quad \begin{aligned} \delta\theta &= 2 \text{ K} \\ r &= 5\sqrt{\left(\frac{x}{L}\right)^2 + \left(\frac{z}{L} - \frac{1}{5}\right)^2} \\ L &= 10 \text{ km} \end{aligned} \quad (87)$$

The hydrostatic background density distribution is computed assuming an ideal gas with constant specific heat capacities and an isentropic exponent of $\gamma = 1.4$, a base density at $z = 0$ of 1 kg/m^3, and a gravitational acceleration of $g = 10 \text{ m/s}^2$. Contours of the initial potential temperature distribution are displayed in Fig. 3.

The test with a smoothed potential temperature distribution was suggested to us by O. Knoth. See the references, e.g., in [1,34] for a history of this test.

In all computations for these tests the time step was determined by

$$\Delta t = \min(16 \text{ s}, \text{CFL}\Delta x / \max_{\Omega}(|u|, |w|)) \quad \text{with} \quad \text{CFL} = 1.0. \quad (88)$$

4.2.2 Results

The flow in this test case is entirely driven by buoyancy forces whose location and strength are determined by the advection of potential temperature. Therefore, one may expect a strong influence of the quality of the
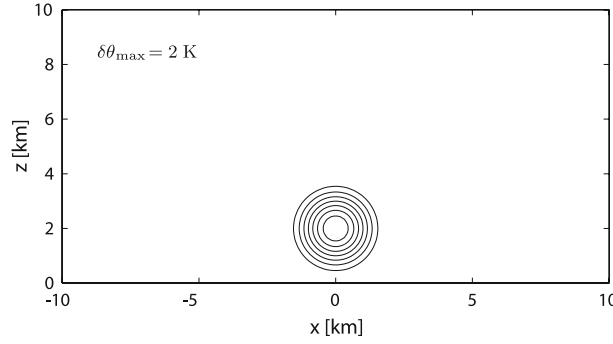
Fig. 3 Initial distribution of potential temperature in the rising plume test case. The contours represent the level sets $\theta = 300\,\text{K} + \{0.25, 0.5, 0.75, 1.0, 1.25, 1.5, 1.75\}\,\text{K}$

advection approximation on the evolving flow field. As time evolves, the "hot bubble" is strongly stretched into a thin sheet, and the solution approaches the limit of resolution on the computational grids used here.

The initial data for this test case are symmetric with respect to the middle vertical axis of the domain, and the initial maximum of potential temperature is located on the symmetry line. Since the boundary conditions, too, are set up mirror-symmetrically, the solution should maintain the symmetry, the maximum should remain located on the symmetry line, and it should not decrease. Yet, Fig. 4a), which displays the potential temperature distribution as computed at $t_1 = 1\,000$ s in our reference run on a grid with 160×80 equally spaced cells and using the sharpened van Leer's limiter with $k = 2$, exhibits two local extrema located symmetrically some finite distance away from the centerline. By that time, the initial maximal excess potential temperature of $\delta\theta_{\max}(0) = 2$ K above the constant background value of 300 K has decayed to $\delta\theta_{\max}(t_1) = 1.50$ K, a decrease due to (nonlinear) numerical dissipation of about 25%. The loss in $\theta_{\max}$ may still be acceptable, as our scheme is in conservation form and therefore redistributes the excess thermal energy contained in the hot bubble but does not dissipate it away. The off-axis development of two extrema appears to be more severe, however, as it will affect the flow field through the associated buoyancy forces.

Limiter functions such as (58) are designed to support the maintainance of sharp gradients while avoiding the occurance of new overshoots in advected scalars. They have built-in mechanisms to maintain plateaus of constant values, leading to the undesired "clipping" of extrema, and others to "steepen" fronts against numerical dissipation. Thus one may suspect that the marked separation of two off-axis extrema in the present test case might be the result of (1) the strongest dissipation occuring near the extremum on the axis, and (2) an enhancement of the arising gradients by the "sharpened" van Leer's limiter as applied here. Figure 4b shows the result of a related calculation that differs only in that we have used van Leer's original limiter function, i.e., we set $\psi(r) \equiv 1$ in (58). The distribution of potential temperature is now in fact less peaked towards the off-axis extrema, but these are still prominently visible. Besides, van Leer's limiter is considerably more dissipative, so that the maximum excess of θ beyond the background value is now $\delta\theta_{\max}(t_1) = 1.38$ K corresponding to a loss in the maximum of about 30%.

In avoiding over- and undershoots of advected scalars, TVD limiters do not distinguish plateaus of constant values from the discrete representation of extrema. If, near an extremum, two neighboring cells reach nearly the same value of the scalar, they are treated as a plateau and no overshoot over their common value is allowed in the sequel. That, however, is inappropriate because a smooth extremum, when advected towards one of the two cells, would make that cell attain a new maximum while decreasing the value in the cell left behind.

To investigate the influence of this "clipping" phenomenon on the solution of the present buoyancy-driven flow, we have implemented a preliminary version of an alternative advection scheme. As in PPM, the "piecewise parabolic method" from [14], and extensions thereof, [6], or in a poor man's one-dimensional version of MU, [49], quadratic reconstruction is applied in each grid cell. The reconstruction parabola matches the cell averages in the reconstructed cell and its next neighbors. Edge values of the scalar, to be used in the upwind flux computation from (60) are then determined by imposing, e.g., for $\langle u \rangle > 0$,

$$\Delta t \left(\overline{\rho} \langle u \rangle \phi^{\text{upw}} \right)_{i+\frac{1}{2}}^{n+\frac{1}{2}} = \overline{\rho} \int_{x^*_{i+\frac{1}{2}}}^{x_{i+\frac{1}{2}}} \phi(x)\,\mathrm{d}x \tag{89}$$
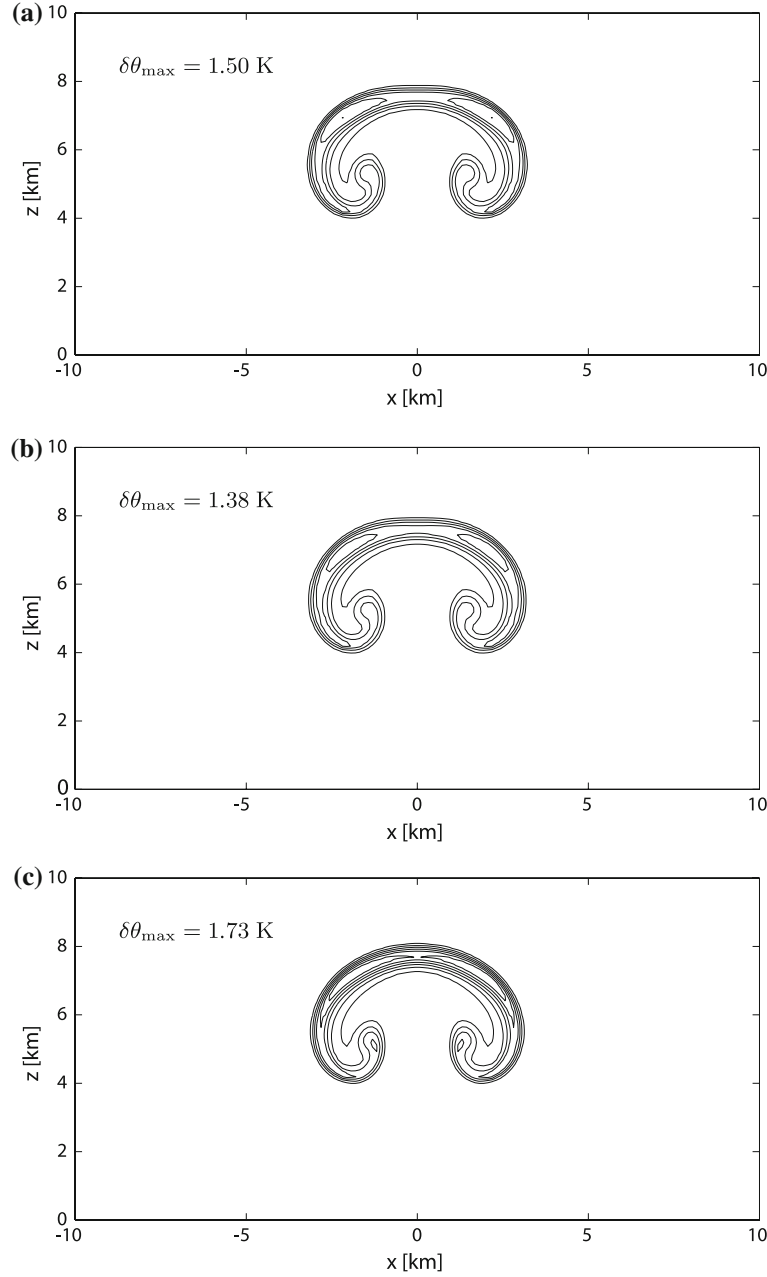
Fig. 4 Potential temperature distributions at time $t = 1\,000$ s for the rising plume test case based on the anelastic model and different options for the advection scheme. Countours every 0.25 K, beginning at 300.25 K. Common numerical parameters: 160×80 grid cells, $(\Delta t)_{\max} = 17$ s, CFL $= 1.0$ otherwise. **a** Piecewise linear MUSCL approach using sharpened van Leer's limiter [$k = 2$ in (58)], **b** same but using original van Leer's limiter [$k = 0$ in (58)], **c** upwind-biased quadratic reconstruction with plateau detection (see Appendix A.2)

where $x^*_{i+\frac{1}{2}}$ is the foot point of the Lagrangian characteristic that arrives at $x_{i+\frac{1}{2}}$ at time t^{n+1}. These upwind-biased reconstruction and half-time predictor steps are used everywhere except where a plateau-indicator switches back to the standard slope-limited piecewise linear reconstruction and prediction described earlier. Importantly, the indicator is designed not to act on cells that carry local extrema. For a detailed description of the scheme as used here see Appendix A2. An extensive study of this method, including rules for determining its free parameters, is deferred to future work.

Figure 4c shows the result of a computation using this "upwind-biased reconstruction with plateau detection". The contours of potential temperature at $t = 1\,000$ s reveal that the tendency to form off-center extrema

is considerably diminished. As expected, the maximum potential temperature is maintained at a much higher level than in the previous runs due to the absence of the clipping phenomenon from the advection scheme. In fact, $\delta\theta_{\max}(t_1) = 1.73$ K which corresponds to a loss in the maximum of 13.5% only. Considering that, by this time, the peak of potential temperature in a vertical slice is squeezed to merely 5–7 grid points, this is quite an acceptable level of dissipation.

Maintainance of symmetry. In all computations shown above, mirror symmetry with respect to the middle vertical axis of the domain is maintained up to relative deviations of the order of 3×10^{-4} in all variables. If instead of the smooth van Leer's limiter and its sharpened version we use, e.g., Sweby's or the Superbee limiter, [40,52], which have built-in switches besides the clipping near extrema, symmetry is much more severely affected (not shown). These observations and the fact that van Leer's original limiter is much more dissipative than the Sweby and Superbee limiters motivated us to suggest the sharpened versions of van Leer's limiter function. Using the upwind biased-quadratic reconstruction, symmetry is maintained to relative errors below 1×10^{-7}.

4.3 Falling drop of cold air

Here, we demonstrate how solutions to the anelastic and pseudo-incompressible model equations deviate from each other at small scales for increasing variation of the potential temperature. The results for the pseudo-incompressible model are more reliable for the cases with large density variation, because this model approaches the zero Mach number variable density flow equations in this regime. In contrast, the anelastic model approaches the Boussinesq approximation for an incompressible fluid, which is valid only in the limit of small potential temperature variations.

4.3.1 Description of the test case

In a small rigid box of dimensions -10 m $\leq x \leq 10$ m, $0 \leq z \leq 10$ m filled with a neutrally stratified ideal gas with constant specific heat capacities which is at rest initially we embed cold, circular "droplets" of air, with increasing initial potential temperature perturbations. The potential temperature initial data read

$$\theta(0, x, z) = 300 \text{ K} - \begin{cases} \dfrac{\delta\theta}{2}\left(1 + \cos(\pi r^2)\right) & (r \leq 1) \\ 0 & \text{otherwise} \end{cases}, \quad \begin{aligned} \delta\theta &= 30, 150, 270 \text{ K} \\ r &= 5\sqrt{\left(\tfrac{x}{L}\right)^2 + \left(\tfrac{z}{L} - 0.7\right)^2} \\ L &= 10 \text{ m} \end{aligned} \tag{90}$$

In all computations for these tests the time step was determined by

$$\Delta t = \min(0.04 \text{ s}, \text{CFL}\,\Delta x / \max_{\Omega}(|u|, |w|)) \quad \text{with} \quad \text{CFL} = 0.9. \tag{91}$$

4.3.2 Results

Figure 5 displays results for the anelastic model in the left column, and for the pseudo-incompressible in the right. From top to bottom the minimum of the potential temperature in the cold air bubble at time $t = 0.0$ is 270, 150, and 30 K, respectively. There are two mechanisms of baroclinicity that distort the originally circular cold air bubble. The first is due to horizontal variations of the buoyancy force, and this effect is active in both the anelastic and pseudo-incompressible models. Its influence is seen prominently in the left column of graphs in Fig. 5, which shows the simulation results for the anelastic (or Boussinesq) model. For this model, the first of the two baroclinic effects is the only relevant process distorting the droplet. The flow induced by the heavy cold air displacing the warmer surrounding air induces a vortex pair that tends to stretch the bubble into a thin sheet in a similar way as seen in the rising bubble test case of Sect. 4.2.

The second baroclinic effect is due to the nonlinearity of the pressure gradient term, $\theta\nabla\pi$, found both in the pseudo-incompressible and in the full compressible model. This term gives rise to a vorticity production term proportional to $\nabla\theta \times \nabla\pi$. There is a pressure maximum at the bottom of the bubble and the pressure drops continuously towards its sides. This pressure drop interacts with the outward pointing potential temperature gradient to induce positive vorticity on the right and negative vorticity on the left side of the cold air patch.
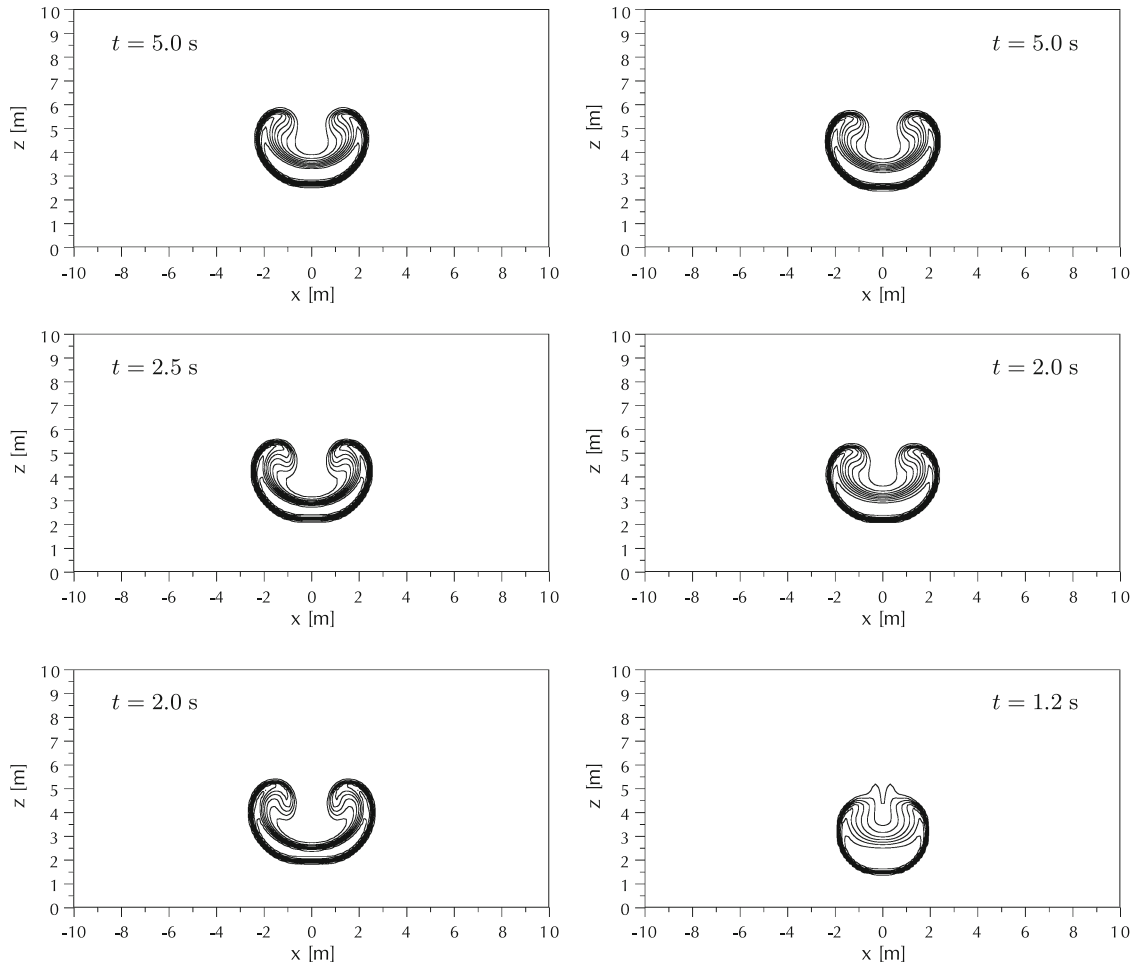
Fig. 5 Falling "droplets" of cold air simulated based on Bannon's anelastic model (*left column*) and Durran's pseudo-incompressible model (*right column*). *Top row* $\theta_{min}/\theta_{max} = 0.9$, *middle row* $\theta_{min}/\theta_{max} = 0.5$, *bottom row* $\theta_{min}/\theta_{max} = 0.1$. Contours are equally spaced at 1/10 of the maximum potential temperature difference in the initial data

These sheets of vorticity imply a jet-like flow of the surrounding air around the bubble, and this tends to counteract the stretching associated with the first mechanism. The pseudo-incompressible model includes this second effect of baroclinic torque and the right column in Fig. 5 shows that for very heavy air in the cold pocket this vorticity generation mechanism even overcomes the stretching effect.

For the small 10% potential temperature perturbation, the results from the anelastic and pseudo-incompressible models are again hardly distinguishable (see the top row of graphs in Fig. 5). This corroborates one of our main conclusions: for density, or potential temperature, variations characteristic of typical meteorological applications, the anelastic and pseudo-incompressible models are equally viable sound-proof model alternatives.

All calculations for the falling cold drop were performed with our standard scheme using the sharpened van Leer's limiter with $k = 2$.

5 Conclusions and open issues

5.1 Conclusions

We have pointed out that the anelastic and pseudo-incompressible models by Bannon [4], and Durran [16], respectively, are structurally very close to the compressible flow equations. Moreover, for length scales small compared with the pressure scale height, both models are asymptotically consistent with the full compressible flow equations as the Mach number vanishes. Whereas Bannon's anelastic model reduces to the Boussinesq

equations in this limit, the pseudo-incompressible model becomes asymptotically equivalent to the zero Mach number incompressible flow equations. The pseudo-incompressible model is therefore more generally applicable than the anelastic model as it correctly captures incompressible flows with large density variations. However, for the small density variations characteristic of flows in the atmosphere and oceans, both models yield virtually indistinguishable results. In agreement with Smolarkiewicz and Dörnbrack [43], we find that differences in flow simulations induced by using either of these models in meteorologically relevant regimes are much smaller than the differences encountered when one and the same set of model equations is solved using different (second order accurate) numerical schemes.

We have proposed a numerical scheme for solving the anelastic and pseudo-incompressible model equations using a formulation that exploits the close structural similarities between the compressible and sound-proof models. The scheme is relatively simple, employing more or less standard Godunov-type second-order techniques, and directional operator splitting. It features two projections per time step for the advective fluxes across grid cell interfaces, and for the cell-centered velocities. Since the scheme is quite insensitive to loose control of the divergence constraints, it is nevertheless quite efficient. Its extension to a semi-implicit solver for the full compressible flow equations should thus be relatively straightforward. A major challenge in this context will be to devise a scheme that integrates long-wave acoustic and internal gravity wave modes accurately with time steps determined by the advection Courant number, see, e.g., [13,20,25,27,36] for related discussions and already proposed schemes.

Another interesting route of numerics development is a relatively simple advection scheme based on upwind-biased parabolic reconstruction, which is constrained solely near plateaus of the advected scalar to a standard TVD-limited piecewise linear distribution. A preliminary implementation of the scheme does not clip extrema and performs well in advecting smooth and non-smooth distributions. Using this scheme we demonstrated that some disturbing perturbations of flow symmetries in the rising bubble test case observed with our standard scheme were due to the clipping of extrema by the second-order TVD schemes.

5.2 Open issues

Consistent with earlier findings, [26], our analysis has revealed that neither the anelastic nor the pseudo-incompressible model can be derived self-consistently through classical scale analysis or formal asymptotics. The reason is an asymptotic time scale separation between advection and internal waves that occurs for realistic stratifications. Only on length scales small compared with the pressure scale height is there asymptotic agreement between the compressible flow equations in the low Mach number limit and the sound-proof models as pointed out above. The reason is that the characteristic internal wave time scale becomes comparable to the advection time even in the presence of large density variations in the small-scale limit, i.e., the time scale separation between advection and internal waves disappears.

For length scales comparable to the pressure scale height, the leading-order theory for the shorter internal wave time scale in a multiscale analysis is a linear model, [28]. Adding the nonlinear advection terms to this leading-order model would amount to formally increasing its accuracy by including terms that arise for the first time in the first-order expansions. Such a model would likely be very similar, if not identical, to the anelastic and pseudo-incompressible models in suitable regimes for the stratification. However, whether it is justifiable to use such a model over the longer advection time scale, i.e., over the time scale within which the higher-order terms can accumulate order $O(1)$ effects, remains an open question.

A Appendix

A.1 Influence of the divergence control

Here, we provide a semi-heuristic explanation for why the scheme presented in this paper is relatively robust with respect to loose divergence controls. The reader may also want to consult [6] for related discussions and further references.

Advection. For $\phi \equiv 1$, in either the pseudo-incompressible or the anelastic model, the relevant conservation law reads

$$\hat{\rho}_t + \nabla \cdot (\hat{\rho} \boldsymbol{v}) = 0, \tag{92}$$

and the predictor step will generally yield a non-zero update $\hat{\rho}_{i,j}^{n+1,*} - \hat{\rho}_{i,j}^n \neq 0$. Even if the velocity field is essentially divergence-free at the beginning of a time step, the density differences within each individual directional operator split step may be large.

To properly represent advection of $\phi \not\equiv 1$ through a conservative finite volume discretization, it is essential that these intermediate density updates are accounted for. As in compressible flow schemes, only the combined updates for $\hat{\rho}$ and $\hat{\rho}\phi$, i.e.,

$$
\begin{aligned}
\hat{\rho}_i^{n+1} - \hat{\rho}_i^n &= -\frac{\Delta t}{\Delta x} \left((\hat{\rho} u)_{i+\frac{1}{2}}^{n+\frac{1}{2}} - (\hat{\rho} u)_{i-\frac{1}{2}}^{n+\frac{1}{2}} \right) \\
(\hat{\rho}\phi)_i^{n+1} - (\hat{\rho}\phi)_i^n &= -\frac{\Delta t}{\Delta x} \left((\hat{\rho} u)_{i+\frac{1}{2}}^{n+\frac{1}{2}} \phi_{i+\frac{1}{2}}^{n+\frac{1}{2}} - (\hat{\rho} u)_{i-\frac{1}{2}}^{n+\frac{1}{2}} \phi_{i-\frac{1}{2}}^{n+\frac{1}{2}} \right),
\end{aligned}
\tag{93}
$$

yield a proper approximation to the advection equation for ϕ.

To be more specific, let us compare the results for $\phi_i^{n+1} - \phi_i^n$ if we do and do not account for the divergence of $\hat{\rho} u$ and the associated changes in $\hat{\rho}$. If we do account for the changes in $\hat{\rho}$, then we know from standard analyses for compressible flow schemes in conservation form that (93) yields a second-order accurate approximation to $\phi_t + u\phi_x = 0$, no matter what the divergence of $\hat{\rho} u$, provided the flux terms $(\hat{\rho} u)_{i+\frac{1}{2}}^{n+\frac{1}{2}}, \phi_{i+\frac{1}{2}}^{n+\frac{1}{2}}$ are calculated with sufficient accuracy. In contrast, if we do not account for the changes of $\hat{\rho}$, i.e., in computing ϕ we assume $\hat{\rho}_i^n \equiv \overline{\hat{\rho}} = \text{const}$, then we find

$$\frac{(\hat{\rho}\phi)_i^{n+1}}{\overline{\hat{\rho}}} - \frac{(\hat{\rho}\phi)_i^n}{\overline{\hat{\rho}}} = -\frac{1}{\hat{\rho}_i^{n+1}} \frac{\Delta t}{\Delta x} \left(\overline{\hat{\rho} u}_i^{n+\frac{1}{2}} \left(\phi_{i+\frac{1}{2}}^{n+\frac{1}{2}} - \phi_{i-\frac{1}{2}}^{n+\frac{1}{2}} \right) + \overline{\phi}_i^{n+\frac{1}{2}} \left((\hat{\rho} u)_{i+\frac{1}{2}}^{n+\frac{1}{2}} - (\hat{\rho} u)_{i-\frac{1}{2}}^{n+\frac{1}{2}} \right) \right). \tag{94}$$

Any divergence $(\hat{\rho} u)_{i+\frac{1}{2}}^{n+\frac{1}{2}} - (\hat{\rho} u)_{i-\frac{1}{2}}^{n+\frac{1}{2}} \neq 0$ will induce an order $O(1)$ error in the advection of ϕ. In (94) we have used the notation

$$\overline{X}_i^{n+\frac{1}{2}} = \frac{1}{2} \left(X_{i+\frac{1}{2}}^{n+\frac{1}{2}} + X_{i-\frac{1}{2}}^{n+\frac{1}{2}} \right), \tag{95}$$

with $X \in \{\hat{\rho} u, \phi\}$. See also the closely related discussion and analysis of the differences between an Eulerian conservative scheme and a non-conservative semi-Lagrange method in [44].

These considerations explain why the use of directional operator splitting in the predictor step does not induce major errors, even though the derivatives $\partial \hat{\rho} u / \partial x$ and $\partial \hat{\rho} w / \partial z$ may be large individually. As another consequence, a relatively weak control of the flux divergence in the MAC-projection may be adopted within the present approach without inducing sizeable errors in the potential temperature field (see the discussion in Sect. 4.1).

Momentum balance. Even if advection is represented robustly, the simulated velocity field may nevertheless be affected by how tight a control on the flow divergence is maintained through the influences of the gravity and pressure gradient terms. Consider the evolution equation for velocity in the pseudo-incompressible model, with the Exner variable, π, used to represent the effect of the pressure gradient,

$$\boldsymbol{v}_t + \boldsymbol{v} \cdot \nabla \boldsymbol{v} + \frac{1}{\Gamma} \theta \nabla \pi = -g \boldsymbol{k}. \tag{96}$$

The equation does not involve any explicit dependence on $\hat{\rho} = \overline{\rho \theta}$. The present scheme respects this scaling in that all momentum increments (55), (65), (70), and (78) involve density weights corresponding to the value of the density variable $\hat{\rho}$ as computed from the scheme at the respective stage of the algorithm, and not the fixed value given by the background stratification.

Yet, the (pseudo-)density, $\hat{\rho}$, does enter the velocity equation indirectly through the pressure gradient term, $\theta \nabla \pi$, because the pressure equation involves the density in a non-trival way. For, say, the pseudo-incompressible model we have $\nabla \cdot (\overline{\rho \theta} \boldsymbol{v}) = 0$, and multiplying (96) by $\overline{\rho \theta}$ and taking the divergence yields

$$\frac{1}{\Gamma} \nabla \cdot (\theta \nabla \pi) + \nabla \cdot (\boldsymbol{v} \cdot \nabla \boldsymbol{v}) = -\frac{1}{\overline{\rho \theta}} \nabla \overline{\rho \theta} \cdot \left(\frac{\theta}{\Gamma} \nabla \pi + g \boldsymbol{k} + (\boldsymbol{v} \cdot \nabla \boldsymbol{v}) \right) \tag{97}$$

The background stratification of $\overline{\rho \theta}$ enters through its logarithmic derivative only. Errors in $\overline{\rho \theta}$ will thus affect the flow field, though relatively weakly.

A.2 Advection based on quadratic reconstruction and plateau detection

Here is the advection scheme outlined briefly in Sect. 4.2.2 for one-dimensional advection at constant velocity, i.e., for

$$u_t + a u_x = 0, \quad (a \equiv \text{const.}) \tag{98}$$

No plateau detected in the neighborhood cell i. For, say, the ith grid cell at time t^n, we fit a parabola $u_i^n(x)$ that has the same mean as the current computational cell-averages in three adjacent cells, so that

$$\frac{1}{\Delta x} \int_{x_{k-\frac{1}{2}}}^{x_{k+\frac{1}{2}}} u_i^n(x)\, dx = u_k^n \quad (k \in \{i-1, i, i+1\}). \tag{99}$$

The cell-interface value of u that enters the flux evaluation at $x_{i+\frac{1}{2}}$ then reads

$$u_{i+\frac{1}{2}}^{n+\frac{1}{2}} = \frac{1}{|a|\Delta t} \int_{x_{i+\frac{1}{2}} - a\Delta t}^{x_{i+\frac{1}{2}}} u_{i*}^n(x)\, dx \quad \text{where} \quad i^* = \begin{cases} i & (a \geq 0) \\ i-1 & (a < 0) \end{cases}. \tag{100}$$

Plateau detected in the neighborhood of cell i. In this case, the reconstruction of left and right cell-interface values within cell i procedes according to the standard MUSCL scheme. We have used the sharpened van Leer limiter with $k = 2$ in conjunction with the piecewise parabolic scheme.

Plateau detection. A plateau is considered detected in the vicinity of cell i if

$$\left(|u_{i-1}^n - u_{i-2}^n| < \epsilon \right) \quad \text{or} \quad \left(|u_{i+2}^n - u_{i+1}^n| < \epsilon \right) \tag{101}$$

where the ϵ is a degree of freedom that we have chosen in an ad-hoc manner so far. For the results in Sect. 4.2.1 and below, we have used $\epsilon = 0.02\sqrt{\Delta x}(\max_i(u) - \min_i(u))$.

We leave a more thorough discussion for future work. To provide an impression of the performance of the various advection schemes used in this paper, we have advected the following distribution, including a top-hat, a triangular wedge, a smooth $1 - \cos(\ )$ hump and a truncated parabola over 10 cycles in a periodic box (see also [11] and references therein),

$$u(0, x) = \sum_{i=1}^{4} U^{(k)}((x - x^{(k)})/\sigma)) \quad (-0.5 \leq x \leq 0.5; \, \sigma = 0.075) \tag{102}$$

with individual shapes given by

$$\begin{aligned} U^{(1)}(x) &= H(1 - \xi) \\ U^{(2)}(x) &= \cos^2(\pi \xi / 2) \\ U^{(3)}(x) &= 1 - \xi \\ U^{(4)}(x) &= 1 - \xi^3, \end{aligned} \quad \text{where} \quad \xi = \min(1, |x|/\sigma) \tag{103}$$

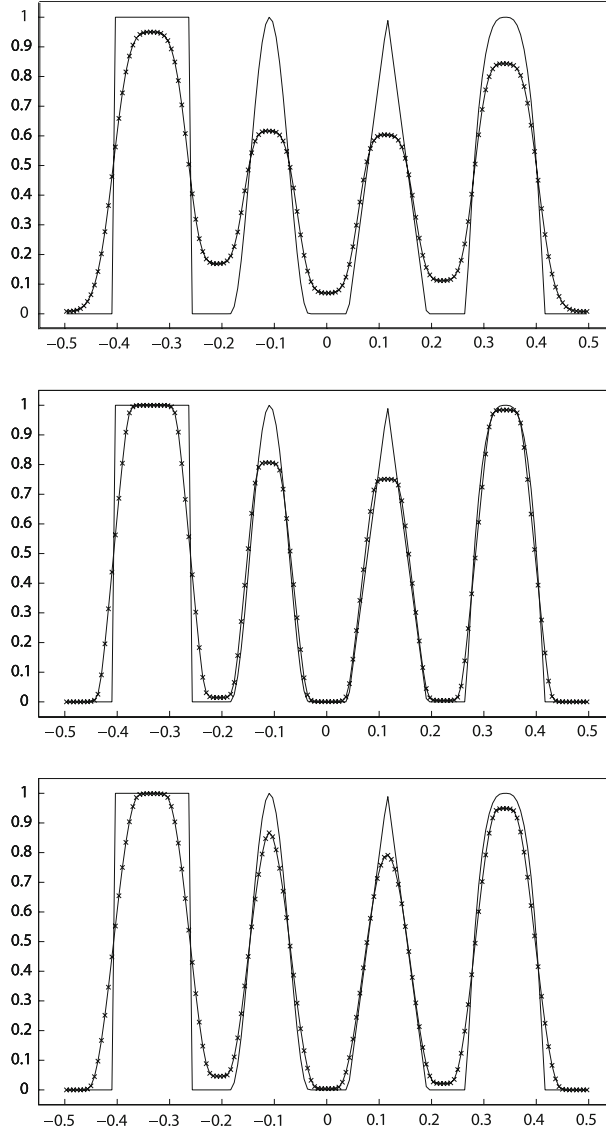and $x^{(1)}, x^{(2)}, x^{(3)}, x^{(4)} = \sigma(-4.5, -1.5, 1.5, 4.5)$.

Fig. 6 Results for the advection of the periodic test distribution from (102) after 10 cycles, 150 grid cells, CFL = 0.5. *Top* MUSCL-scheme with van Leer's original limiter [$k = 0$ in (58)], *middle* sharpened van Leer's limiter [$k = 2$ in (58)], *bottom* parabolic reconstruction with plateau decection

Figure 6 shows results for CFL = 0.5 which, due to the directional operator splitting used in the full implementation of the sound-proof model solvers, is the effective Courant number for the simulations in Sect. 4. For CFL = 0.9, the results improve for all three schemes, but the piecewise parabolic method with plateau detection performs especially well (see Fig. 7).

A.3 Advection observing a maximum principle

Here we prove that, with two modifications, the scheme presented here obeys a maximum principle for potential temperature (or any other advected scalar) provided the following two CFL-like conditions are satisfied,

$$\frac{m_+}{\hat{\rho}_i^n} = \frac{\lambda}{\hat{\rho}_i^n} \left| \left(\hat{\rho} \langle u \rangle \right)_{i+\frac{1}{2}}^{n+\frac{1}{2}} \right| < \frac{1}{2} \quad \text{and} \quad \frac{\lambda}{\hat{\rho}_i^n} \left(\left(\hat{\rho} \langle u \rangle \right)_{i+\frac{1}{2}}^{n+\frac{1}{2}} - \left(\hat{\rho} \langle u \rangle \right)_{i-\frac{1}{2}}^{n+\frac{1}{2}} \right) \leq \frac{1}{2}. \tag{104}$$

With each sub-step satisfying these conditions, we essentially recover $u \, \Delta t / \Delta x \leq 1$ for a full Strang splitting cycle as it involves two sub-steps for each coordinate direction.
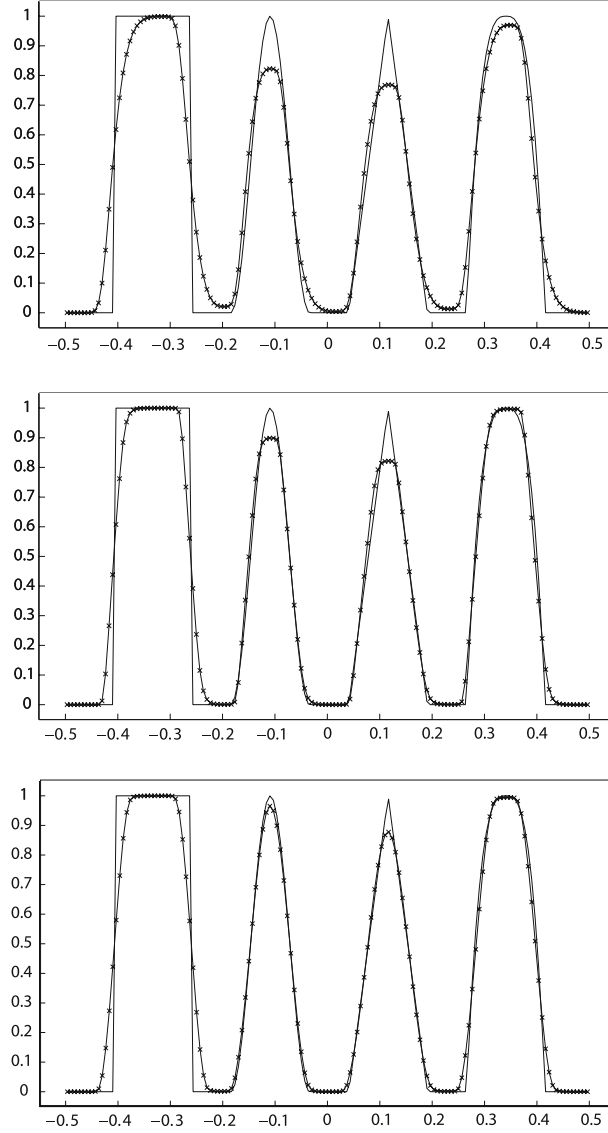
Fig. 7 Same as Fig. 6, but at CFL = 0.9

The two modifications that we assume here are

1. Replace $(1 - \lambda u_i^n)$ and $(1 + \lambda u_{i+1}^n)$ in (56) with $(1 - \max(0, \lambda u_i^n))$ and $(1 + \min(0, \lambda u_{i+1}^n))$, respectively (see Colella and Glaz [12])
2. Use standard TVD slope limiting instead of the special construction for reconstruction near extrema from (57).

While the scheme in this version obeys a maximum principle as will be shown shortly, it is also considerably more dissipative.

Before we procede, we observe that the pre-factors of $s_i^{n,\pm}$ in (56) now satisfy

$$0 \leq \left(1 - \max\left(0, \lambda u_i^n\right)\right), \quad \left(1 + \min(0, \lambda u_{i+1}^n)\right) \leq 1, \tag{105}$$

provided the standard CFL condition $\lambda u_i^n \leq 1$ is imposed. As a consequence, the spatio-temporal reconstruction satisfies the maximum principle,

$$\phi_{i+\frac{1}{2}}^{n+\frac{1}{2},\pm} \in \left[\min\left(\phi_i^n, \phi_{i+1}^n\right), \max\left(\phi_i^n, \phi_{i+1}^n\right)\right], \tag{106}$$

if the slope limiter is of TVD type.

The analysis now procedes in two steps. First, we follow Larrouturou [30] in demonstrating that each directional operator split step of the explicit predictor obeys the maximum principle. By the design of the characteristics-based update to the half-time level $t^{n+\frac{1}{2}}$ for flux evaluations, we are able to prove a maximum principle even for the full second-order accurate scheme. Larrouturou, using a different half-time predictor, could only establish the maximum principle rigorously for the spacially second-order, but temporally first-order accurate scheme.

In the second step, we prove a maximum principle for the flux corrections induced by the MAC-projection.

One-dimensional advection predictor. The general one-dimensional predictor sub-step from (55) when specialized for a scalar advected quantity, ϕ, reads

$$(\hat{\rho}\phi)_i^{n+1} = (\hat{\rho}\phi)_i^n - (m_+\phi_+ - m_-\phi_-) . \tag{107}$$

The update for the density variable, $\hat{\rho}$, is obtained for $\phi \equiv 1$, i.e.,

$$\hat{\rho}_i^{n+1} = \hat{\rho}_i^n - (m_+ - m_-). \tag{108}$$

where

$$m_\pm = \lambda \, (\hat{\rho}\langle u\rangle)_{i\pm\frac{1}{2}}^{n+\frac{1}{2}}, \quad \phi_\pm = (\phi^{\text{upw}})_{i\pm\frac{1}{2}}^{n+\frac{1}{2}} \tag{109}$$

Case 1 $m_+m_- \geq 0$

When both mass fluxes are positive, we have

$$\phi_i^{n+1} = \frac{a \, \phi^* + m_-\phi_-}{a + m_-} \tag{110}$$

where

$$a = \left(\hat{\rho}_i^n - m_+\right), \tag{111}$$

and

$$\phi^* = \frac{1}{a} \left(\hat{\rho}_i^n \, \phi_i^n - m_+\phi_+\right) \tag{112}$$

If $a \geq 0$, then (110) yields the new time level value, ϕ_i^{n+1}, of the advected scalar as a convex combination of ϕ^* and ϕ_-. We will rely on this property below, so we adopt the condition $a \geq 0$ as the first CFL-like criterion under *Case 1*.

Next, we rewrite ϕ^* as

$$\phi^* = \phi_i^n + \frac{m_+}{a} \left(\phi_i^n - \phi_+\right), \tag{113}$$

and require that

$$\frac{m_+}{a} < 1, \tag{114}$$

which (1) guarantees $a > 0$ making (110) a convex combination, and (2) amounts to the first CFL-like condition from (104)

$$\frac{m_+}{\hat{\rho}_i^n} = \frac{\lambda(\hat{\rho}\langle u\rangle)_{i+\frac{1}{2}}^{n+\frac{1}{2}}}{\hat{\rho}_i^n} < \frac{1}{2}. \tag{115}$$

We recall from (56) that, in the present *Case 1*,

$$\phi_i^n - \phi_+ = -\frac{\Delta x}{2} \left(1 - \max\left(0, \lambda u_i^n\right)\right) s_i^n \tag{116}$$

with

$$s_i^n = \left(\partial_x^{\lim}\phi\right)_i^n ,\tag{117}$$

and conclude from (105) and (113), (114) that

$$\phi^* \in \left[\min\left(\phi_i^n, \phi_i^n - \frac{\Delta x}{2} s_i^n\right), \max\left(\phi_i^n, \phi_i^n - \frac{\Delta x}{2} s_i^n\right)\right].\tag{118}$$

But, since s_i^n is a TVD-limited slope it follows that

$$\phi^* \in \left[\min\left(\phi_i^n, \phi_{i-1}^n\right), \max\left(\phi_i^n, \phi_{i-1}^n\right)\right].\tag{119}$$

According to (106) ϕ_- belongs to the same interval, and so will ϕ_i^{n+1}, being a convex combination of ϕ^* and ϕ_-. This establishes the maximum principle for scalar advection under the CFL condition (114) when the mass fluxes across the adjacent cell interfaces are either both positive or both negative.

The analysis for the case of negative m_+ and m_- is proceeds analogously.

Case 2 $m_+ < 0; \quad m_- > 0$

In that case,

$$\phi_i^{n+1} = \frac{\hat{\rho}_i^n \phi_i^n + |m_+|\phi_+ + |m_-|\phi_-}{\hat{\rho}_i^n + |m_+| + |m_-|}\tag{120}$$

is immediately identified as a convex combination of scalar values which, by design of the spatio-temporal reconstruction, lie within the range of $\left[\min\left(\phi_{i-1}^n, \phi_i^n, \phi_{i+1}^n\right), \max\left(\phi_{i-1}^n, \phi_i^n, \phi_{i+1}^n\right)\right]$.

This establishes the maximum principle for *Case 2*.

Case 3 $m_+ > 0; \quad m_- < 0$

The argument here is similar to that for *Case 1*. We first write

$$\phi_i^{n+1} = \frac{\hat{\rho}_i^n \phi_i^n - |m_+|\phi_+ - |m_-|\phi_-}{\hat{\rho}_i^n - |m_+| - |m_-|}\tag{121}$$

Next we require that

$$\frac{\hat{\rho}_i^{n+1}}{\hat{\rho}_i^n} \geq \frac{1}{2}\tag{122}$$

which is effectively the second of the CFL-like conditions on the *mass flux divergence* from (104) because, due to the signs of $m_\pm$ in the present *Case 3*, it implies

$$\frac{|m_+| + |m_-|}{\hat{\rho}_i^{n+1}} \leq 1 \quad \text{and} \quad \frac{\lambda}{\hat{\rho}_i^n}\left((\hat{\rho}\langle u\rangle)_{i+\frac{1}{2}}^{n+\frac{1}{2}} - (\hat{\rho}\langle u\rangle)_{i-\frac{1}{2}}^{n+\frac{1}{2}}\right) \leq \frac{1}{2}.\tag{123}$$

Rewriting (121) as

$$\phi_i^{n+1} = \phi_i^n + \frac{1}{\hat{\rho}_i^{n+1}}\left(|m_+|\left[\phi_i^n - \phi_+\right] + |m_-|\left[\phi_i^n - \phi_-\right]\right)\tag{124}$$

and noticing that, due to the upwinding procedure at the cell interfaces,

$$\begin{aligned}
\phi_i^n - \phi_- &= \frac{\Delta x}{2}\left(1 + \min\left(0, \lambda u_i^n\right)\right) s_i^n \\
\phi_i^n - \phi_+ &= \frac{\Delta x}{2}\left(-1 + \max\left(0, \lambda u_i^n\right)\right) s_i^n
\end{aligned}\tag{125}$$

we can cast the (124) into

$$\phi_i^{n+1} = \phi_i^n + \xi \, \frac{\Delta x}{2} \, s_i^n \tag{126}$$

where

$$\xi = \frac{|m_+| + |m_-|}{\hat{\rho}_i^{n+1}} \left(\frac{|m_+|}{|m_+| + |m_-|} \left(1 + \min\left(0, \lambda u_i^n\right)\right) + \frac{|m_-|}{|m_+| + |m_-|} \left(-1 + \max\left(0, \lambda u_i^n\right)\right) \right). \tag{127}$$

According to (123), the first factor in this defintion is less than or equal to unity, whereas the bracket contains a convex combination of two numbers from the interval $[-1, 1]$. It follows that

$$\xi \in [-1, 1]. \tag{128}$$

Furthermore, with s_i^n being a TVD-limited slope we conclude from (126) that

$$\phi_i^{n+1} \in \left[\min\left(\phi_{i-1}^n, \phi_i^n, \phi_{i+1}^n\right), \max\left(\phi_{i-1}^n, \phi_i^n, \phi_{i+1}^n\right)\right]. \tag{129}$$

This establishes the maximum principle for *Case 3*.

MAC projection. In the first projection, all advective fluxes are determined from the mass flux corrections via first-order upwinding. For an advected scalar, ϕ, the MAC correction from (74) may be written as

$$\phi_{i,j}^{n+1} = \frac{a \, \phi_{i,j}^{n+1,*} + \sum\limits_{m_{\boldsymbol{\nu}} < 0} |m_{\boldsymbol{\nu}}| \phi_{i+\mu, j+\nu}^{n+1,*}}{a \, + \sum\limits_{m_{\boldsymbol{\nu}} < 0} |m_{\boldsymbol{\nu}}|}. \tag{130}$$

Here

$$a = \hat{\rho}_{i,j}^{n+1,*} - \sum\limits_{m_{\boldsymbol{\nu}} \geq 0} m_{\boldsymbol{\nu}}, \tag{131}$$

$\boldsymbol{\nu} = (\mu, \nu) \in \{ (-1, 0), \ (0, -1), \ (1, 0), \ (0, 1) \}$ is a multi-index, and

$$m_{\boldsymbol{\nu}} = \frac{(\Delta t)^2}{2} \begin{cases} \pm F_{i \pm \frac{1}{2}, j}^{\mathrm{MAC}} & \text{for} \quad \boldsymbol{\nu} = (\pm, 0) \\ \pm G_{i, j \pm \frac{1}{2}}^{\mathrm{MAC}} & \text{for} \quad \boldsymbol{\nu} = (0, \pm) \end{cases}. \tag{132}$$

As long as $a \geq 0$, the update in (130) for $\phi_{i,j}^{n+1}$ is a convex combination of $\phi_{i,j}^{n+1,*}$ and the neighboring values $\phi_{i+\nu, j+\mu}^{n+1,*}$, so that the maximum principle is observed.

The positivity condition on a is another CFL-type constraint to be observed in addition to the ones discussed in the last paragraph. In practice, this latter condition should be less constraining than the previous ones for the explicit predictor, because due to the facts that the predictor step (1) always starts with a divergence-free field, and (2) includes the effect of the old-time level pressure gradient, the divergence corrections in the MAC-projection are merely of order $O((\Delta t)^2)$ for smooth flows.

References

1. Ahmad, N., Lindeman, J.: Euler solutions using flux-based wave decomposition. Int. J. Num. Meth. Fluids **54**, 47–72 (2007)
2. Almgren, A.S., Bell, J.B., Rendleman, C.A., Zingale, M.: Low mach number modeling of type ia supernovae. i. hydrodynamics. Astrophys. J. 922–936 (2006)
3. Almgren, A.S., Bell, J.B., Crutchfield, W.Y.: Approximate projection methods: Part i. inviscid analysis. SIAM J. Sci. Comput. **22**(4), 1139–1159 (2000)
4. Bannon, P.R.: On the anelastic approximation for a compressible atmosphere. J. Atmos. Sci. **53**, 3618–3628 (1996)
5. Bell, J.B., Marcus, D.: A second-order projection method for variable-density flows. J. Comput. Phys. **101**, 334–348 (1992)
6. Blossey, P.N., Durran, D.R.: Selective monotonicity preservation in scalar advection. J. Comput. Phys. **227**, 5160–5183 (2008)

7. Bonaventura, L.: A semi-implicit semi-lagrangian scheme using the height coordinate for a nonhydrostatic and fully elastic model of atmospheric flows. J. Comput. Phys. **158**, 186–213 (2000)
8. Botta, N., Klein, R., Almgren, A.: Asymptotic analysis of a dry atmosphere. In: Proceedings of 3rd ENUMATH, Jyväskylä, Finnland 1999. World Scientific (2000)
9. Botta, N., Klein, R., Almgren, A.S.: Dry atmosphere asymptotics. Technical Report 55, PIK Potsdam Institute for Climate Impact Research, Potsdam (1999)
10. Botta, N., Klein, R., Langenberg, S., Lützenkirchen, S.: Well-balanced finite volume methods for near-hydrostatic flows. J. Comput. Phys. **196**, 539–565 (2004)
11. Cada, M., Torrilhon, M.: Compact third-order limiter functions for finite volume methods. J. Comp. Phys. **228**(11), 4118–4145 (2009)
12. Colella, P., Glaz, H.M.: Efficient solution algorithms for the Riemann problem for real gases. J. Comp. Phys. **59**, 264–289 (1985)
13. Colella, P., Pao, K.: A projection method for low speed flows. J. Comp. Phys. **149**, 245–269 (1999)
14. Colella, P., Woodward, P.R.: The piecewise-parabolic method (PPM) for gasdynamical simulations. J. Comput. Phys. **54**, 174–201 (1984)
15. Davies, T., Staniforth, A., Wood, N., Thuburn, J.: Validity of anelastic and other equation sets as inferred from normal-mode analysis. Q. J. Roy. Meteorol. Soc. **129**, 2761–2775 (2003). doi:10.1256/qj.02.195
16. Durran, D.R.: Improving the anelastic approximation. J. Atmos. Sci. **46**, 1453–1461 (1989)
17. Durran, D.R.: A physically motivated approach for filtering acoustic waves from the equations governing compressible stratified flow. J. Fluid Mech. **601**, 365–379 (2008)
18. Dutton, J.A., Fichtl, G.H.: Approximate equations of motion for gases and liquids. J. Atmos. Sci. **47**, 1794–1798 (1969)
19. Gassmann, A.: An improved two-time-level split-explicit integration scheme for non-hydrostatic compressible models. Meteorol. Atmos. Phys **88**, 23–38 (2005)
20. Gatti-Bono, C., Colella, P.: An anelastic allspeed projection method for gravitationally stratified flows. J. Comp. Phys. **216**, 589–615 (2006)
21. Giraldo, F.X., Restelli, M.: A study of spectral element and discontinuous galerkin methods for the navier–stokes equations in nonhydrostatic mesoscale atmospheric modeling: equation sets and test cases. J. Comp. Phys. **227**, 3849–3877 (2008)
22. Hundertmark, T., Reich, S.: A regularization approach for a vertical slice model and semi-lagrangian stoermer-verlet time-stepping. Q. J. R. Meteorolog. Soc. **133**, 1575–1587 (2007)
23. Janjic, Z.I., Gerrity, J.P., Nickovic, S.: An alternative approach to nonhydrostatic modeling. Mon. Weather Rev. **129**, 1164–1178 (2001)
24. Kadioglu, S.Y., Klein, R., Minion, M.L.: A fourth-order auxiliary variable projection method for zero-mach number gas dynamics. J. Comp. Phys. **227**(3), 2012–2043 (2008)
25. Klein, R.: Semi-implicit extension of a godunov-type scheme based on low mach number asymptotics i: one-dimensional flow. J. Comput. Phys. **121**, 213–237 (1995)
26. Klein, R.: Asymptotic analyses for atmospherics flows and the construction of asymptotically adaptive numerical methods. Zeitschr. Angew. Math. Mech. **80**, 765–777 (2000)
27. Klein, R., Botta, N., Hofmann, L., Meister, A., Munz, C.-D., Roller, S., Sonar, Th.: Asymptotic adaptive methods for multiscale problems in fluid mechanics. J. Eng. Math. **39**, 261–343 (2001)
28. Klein, R., Majda, A.J.: Systematic multiscale models for deep convection on mesoscales. Theor. Comput. Fluid Dyn. **20**, 525–552 (2006)
29. Klemp, J.B., Skamarock, W.C., Dudhia, J.: Conservative split-explicit time integration methods for the compressible non-hydrostatic equations. Mon. Weather Rev. **135**, 2897–2913 (2007)
30. Larrouturou, B.: How to preserve the mass fraction positivity when computing compressible multi-component flows. J. Comp. Phys. **95**, 59–84 (1991)
31. LeVeque, R.J.: Finite volume methods for hyperbolic problems. Cambridge University Press, Basel (2002)
32. Lipps, F., Hemler, R.: A scale analysis of deep moist convection and some related numerical calculations. J. Atmos. Sci. **29**, 2192–2210 (1982)
33. Majda, A., Klein, R.: Systematic multi-scale models for the tropics. J. Atmos. Sci. **60**, 393–408 (2003)
34. Mendez-Nunez, L.R., Carroll, J.J.: Application of the maccormack scheme to atmospheric nonhydrostatic models. Mon. Weather Rev. **122**, 984–1000 (1994)
35. Munz, C.-D.: On the construction and comparison of two-step schemes for the Euler equations. In: Hirschel, E.H. (eds.) Notes on Numerical Fluid Mechanics, vol. 14, pp. 195–217, Vieweg Verlag, Braunschweig/Wiesbaden (1986)
36. Munz, C.-D., Roller, S., Klein, R., Geratz, K.J.: The extension of incompressible flow solvers to the weakly compressible regime. Comput. Fluids **32**, 173–196 (2003)
37. Ogura, Y., Phillips, N.A.: Scale analysis of deep moist convection and some related numerical calculations. J. Atmos. Sci. **19**, 173–179 (1962)
38. Parkins, C.J., Blythe, P.A., Crighton, D.G.: Hot spot ignition: the newtonian limit. Proc. Roy. Soc. Phys. Eng. Sci. **456**, 2857–2882 (2000)
39. Reisner, J.M., Knoll, D.A., Wyszogradzki, A.A.: An implicitly balanced hurricane model with physics based preconditioning. Mon. Weather Rev. **133**, 1003–1022 (2005)
40. Roe, P.L.: Some contributions to the modeling of discontinuous flows. Lect. Notes Appl. Math. **22**, 163–193 (1985)
41. Schneider, Th., Botta, N., Klein, R., Geratz, K.J.: Extension of finite volume compressible flow solvers to multi-dimensional, variable density zero Mach number flow. J. Comput. Phys. **155**, 248–286 (1999)
42. Schochet, S.: The mathematical theory of low mach number flows. M2AN **39**, 441–458 (2005)
43. Smolarkiewicz, P.K., Dörnbrack, A.: Conservative integrals of adiabatic durran's equations. Int. J. Numer. Meth. Fluids **56**, 1513–1519 (2007)
44. Smolarkiewicz, P.K., Grubisic, V., Margolin, L.G.: On forward-in-time differencing for fluids: stopping criteria for iterative solutions of anelastic pressure equations. Mon. Weather Rev. **125**, 647–654 (1997)

45. Smolarkiewicz, P.K., Margolin, L.G.: Variational solver for elliptic problems in atmospheric flows. Appl. Math. Comp. Sci. **4**, 527–551 (1994)
46. Smolarkiewicz, P.K., Margolin, L.G.: On forward-in-time differencing for fluids: an eulerian/semi-lagrangian non-hydro-static model for stratified flows. Atmos. Ocean Special **XXXV**, 127–152 (1997)
47. Smolarkiewicz, P.K., Margolin, L.G.: Mpdata: a finite-difference solver for geophysical flows. J. Comput. Phys. **140**, 459–480 (1998)
48. Sobel, A., Nilsson, J., Polvani, L.: The weak temperature gradient approximation and balanced tropical moisture waves. J. Atmos. Sci. **58**, 3650–3665 (2001)
49. Stevens, D.E., Bretherton, S.: A forward-in-time advection scheme and adaptive multilevel flow solver for nearly incompressible atmospheric flow. J. Comput. Phys. **129**, 284–295 (1996)
50. Strang, G.: On the construction and comparison of difference schemes. SIAM J. Numer. Anal. **5**, 506–517 (1968)
51. Süli, E.: Convergence of finite volume schemes for poisson's equation on nonuniform meshes. SIAM J. Numer. Anal. **28**(5), 1419–1430 (1991)
52. Sweby, P.K.: High resolution schemes using flux limiters for hyperbolic conservation laws. SIAM J. Numer. Anal. **21**, 995–1011 (1984)
53. Ting, L., Klein, R., Knio, O.M.: Vortex dominated flows: analysis and computation for multiple scales. Series in Applied Mathematical Sciences, vol. 116, Springer Verlag, Berlin (2007)
54. van Leer, B.: Upwind and high-resolution methods for compressible flow: from donor cell to residual-distribution schemes. Comm. Comput. Phys. **1**, 192–206 (2006)
55. Vater, S., Klein, R.: Stability of a cartesian grid projection method for zero froude number shallow water flows. Technical Report 07-13, Konrad-Zuse-Zentrum für Informationstechnik Berlin, Berlin, http://opus.kobv.de/zib/volltexte/2007/956/ (2007)
56. Vater, S., Klein, R.: Stability of a Cartesian grid projection method for zero Froude number shallow water flows. Numer. Math. (2009). doi:10.1007/s00211-009-0224-8
57. Zeytounian, R.K.: Asymptotic modeling of atmospheric flows. Springer, Heidelberg (1990)